RESEARCH ARTICLE

CrossMark

Reconstructing lava flow emplacement histories with rheological and morphological analyses: the Harrat Rahat volcanic field, Kingdom of Saudi Arabia

Hannah R. Dietterich[1] · Drew T. Downs[2] · Mark E. Stelten[2] · Hani Zahran[3]

Abstract

Mafic volcanic fields are widespread, but few have erupted in historic times, providing limited observations of the magnitudes, dynamics, and timescales of lava flow emplacement in these settings. To expand our knowledge of effusive mafic eruptions, we must evaluate solidified flows to discern syn-eruptive conditions. The Harrat Rahat volcanic field in western Saudi Arabia offers a good opportunity for this, with a historical eruption in 1256 CE and many well-preserved prehistoric flows. We combine historical observations and rheological and morphological analyses of the youngest flows with analytical models to reconstruct eruptive histories and lava flow emplacement conditions in Harrat Rahat. Petrologic analysis of samples for emplacement temperatures and crystallinities shows cooling trends from vent to toe of ~ 1140 to ~ 1090 °C at rates of 2–7 °C km^{-1}, crystallinities increasing from 0.5 to 60%, and apparent viscosities increasing from 10^2 to 10^9 Pa s. High-resolution topographic data facilitates quantitative analysis of morphology and interpolation of pre-eruptive surfaces to measure flow thicknesses, channels, and levees, and enables calculation of eruptive volumes. Analytical models relating flow morphology to emplacement conditions are applied to estimate effusion rates. Within the suite of studied flows, volume estimates range from 0.07 to 0.42 km^3 dense rock equivalent, with effusion rates on the order of 10 to 100 s of m^3 s^{-1} and durations from 1 to 15 weeks. These integrated analyses quantify past lava flow emplacement conditions and dynamics in Harrat Rahat, improving our understanding and observations of fundamental parameters and controls of effusive eruptions in mafic volcanic fields.

Keywords ʻAʻā lava flow · Channel morphology · Cooling · Crystallization · Effusion rate

✉ Hannah R. Dietterich
hdietterich@usgs.gov

1 Alaska Volcano Observatory, U.S. Geological Survey, 4230 University Drive Suite 100, Anchorage, AK 99058, USA

2 California Volcano Observatory, U.S. Geological Survey, 345 Middlefield Road, Menlo Park, CA 94025, USA

3 National Center for Earthquakes and Volcanoes, Saudi Geological Survey, P.O. Box 54141, Jeddah 21514, Saudi Arabia

Introduction

Mafic lava flows are the most prevalent volcanic landform on Earth and impact communities around the world (e.g., Walker 2000; Harris 2015; Siebert et al. 2015). Observations of emplacement conditions of these flows are concentrated at volcanic centers with frequent historical activity, but similar observations of the more sporadic eruptions from mafic volcanic fields, of which > 200 have been active during the Holocene, are missing (Siebert et al. 2010). Such volcanic fields are widespread globally and are characterized by distributed volcanism producing numerous, typically monogenetic volcanoes within an area (Valentine and Connor 2015). However, with few historical eruptions (Smith and Németh 2017), the paucity of observations of active flows in these settings has limited our understanding of their magnitudes, rheologies, dynamics, and timescales (Valentine and Connor 2015). Sparse data from observed eruptions such as at Paricutín, Mexico

🖄 Springer

(1943–1952; Foshag and González 1956) demonstrate that effusive eruptions in mafic volcanic fields can be long-lived and produce extensive flows. More recently, geologic studies of prehistoric mafic volcanic field eruptions have begun to characterize these flows and their eruption conditions from flow deposits (e.g., Loock et al. 2010; Chevrel et al. 2016; Deligne et al. 2016; Soldati et al. 2017). However, questions remain about the range of sizes, durations, physical properties, and dynamics of effusive eruptions from mafic volcanic fields, with implications for future flow behavior and impacts (Harris 2015). Observations and analysis of flow emplacement are therefore needed to improve our records, modeling, and understanding of eruptive behavior in these settings.

Studies of active and solidified lava flows, as well as experimental and analytical modeling, have demonstrated the close association between emplacement conditions, lava flow length and advance, and final post-emplacement flow textures and morphology (e.g., Macdonald 1953; Walker 1973; Griffiths 2000). Fundamental emplacement parameters include lava effusion rate, flow rheology, and eruption duration (e.g., Walker 1973; Kilburn and Lopes 1991; Harris et al. 2007a). Past investigations have found that higher effusion rates produce flows with higher advance rates and greater lengths (e.g., Walker 1973; Pinkerton and Wilson 1994; Kauahikaua et al. 2003) and have used channel dimensions to estimate effusion rates based on analytical theory (e.g., Kerr et al. 2006; Chevrel et al. 2013; Soldati et al. 2017). Effusion rate may be characterized for different spatial scales, such as a whole flow field or a local lava channel, and timescales, including an average or mean output rate calculated by dividing the total volume by the duration of the eruption, a time-averaged discharge rate over a period of time, or an instantaneous measure (Harris et al. 2007a). Lava rheology has been experimentally tied to lava temperature and composition (Giordano et al. 2008), as well as to the presence and characteristics of crystals and bubbles (Mader et al. 2013), and is reflected in flow and channel morphology in experiments and natural flows (e.g., Hulme 1974; Kerr et al. 2006; Chevrel et al. 2013; Kolzenburg et al. 2018). We can employ the relationships between lava flow petrology, morphology, and emplacement parameters to quantify the intensities and magnitudes (effusion rates, volumes), rheologies, dynamics, and timescales that control flow behavior, thereby building our understanding of eruptions in mafic volcanic fields.

Morphological and rheological analyses have proved valuable for assessing eruptive volumes at volcanic fields around the world and have offered some of the first results characterizing rheological evolution in these systems (Chevrel et al. 2016; Deligne et al. 2016; Soldati et al. 2017). Applications of flow morphology have largely used coarse cross-sections with detailed rheological analysis (Chevrel et al. 2013, 2016; Kolzenburg et al. 2017; Soldati et al. 2017), or high-spatial-resolution topography without rheology measurements

(Deardorff and Cashman 2012). Integrating analysis of high-spatial-resolution topographic data with petrologic investigations and analytical models of rheology and lava channelization allows us to quantify the properties of past eruptions at such locations.

In this study, we employ this approach for a set of young lava flows in Harrat Rahat volcanic field in western Saudi Arabia. We integrate historical records, mapping, geochemistry, petrologic, and morphologic analysis of these recent lava flows in Harrat Rahat to evaluate their eruption temperatures and initial viscosities, investigate their rheological evolution, and estimate volumes, effusion rates, and durations. We find that these methods work well for characterizing the glassy, well-exposed lavas in Harrat Rahat, and that these flows have broadly similar emplacement conditions to recent mafic lava flows at basaltic shield and stratovolcanoes. Our results suggest that observations from mafic effusive eruptions in a variety of settings can inform the rheology and emplacement dynamics of the less frequent eruptions in mafic volcanic fields.

Geological setting

Harrat Rahat is one of at least 15 continental, intra-plate volcanic fields stretching > 3000 km from Yemen to Turkey (Fig. 1a). Prior mapping has provided total eruptive volume estimates of ~ 2000 km^3, with mafic lava flows making up > 95% of the volcanic strata and the youngest eruptions concentrated in the northernmost part of Harrat Rahat (Camp and Roobol 1989, 1991; Moufti et al. 2012, 2013). New geologic mapping and geochronology have revealed eruption ages ranging from ≥ 1 Ma to a single confirmed historic eruption in 1256 CE (Moufti et al. 2013; Downs et al. 2018; Stelten et al. 2018). Lava flow emplacement in Harrat Rahat has not been investigated using quantitative analyses of morphology or rheology, but the site offers both historic and prehistoric flows, availability of high-spatial-resolution topography, superb exposures and sample access, making it an ideal setting to explore eruptive conditions in mafic volcanic field lavas.

The historic eruption in 1256 CE has been the main focus of past lava flow emplacement studies in Harrat Rahat. Based on historical accounts, this eruption began on June 26, 1256 CE and lasted for 52 days (Al-Samhoody 1486; Camp et al. 1987). It formed seven scoria cones along a ~ 2.25-km-long fissure vent, which sent 0.0077 km^3 of airfall tephra to > 5 km distance (Kawabata et al. 2015), and extruded ~ 0.4 km^3 of chemically heterogeneous alkalic and tholeiitic basalt, which flowed ~ 23 km from the vent (Kereszturi et al. 2016). The products of this eruption are named the "basalt of al Labah" on a new geologic map of the northern end of the volcanic field (Downs et al. 2018), and are termed the 1256 CE flow field in this paper for simplicity (Fig. 1b). Descriptions of the geochemical evolution, flow surface
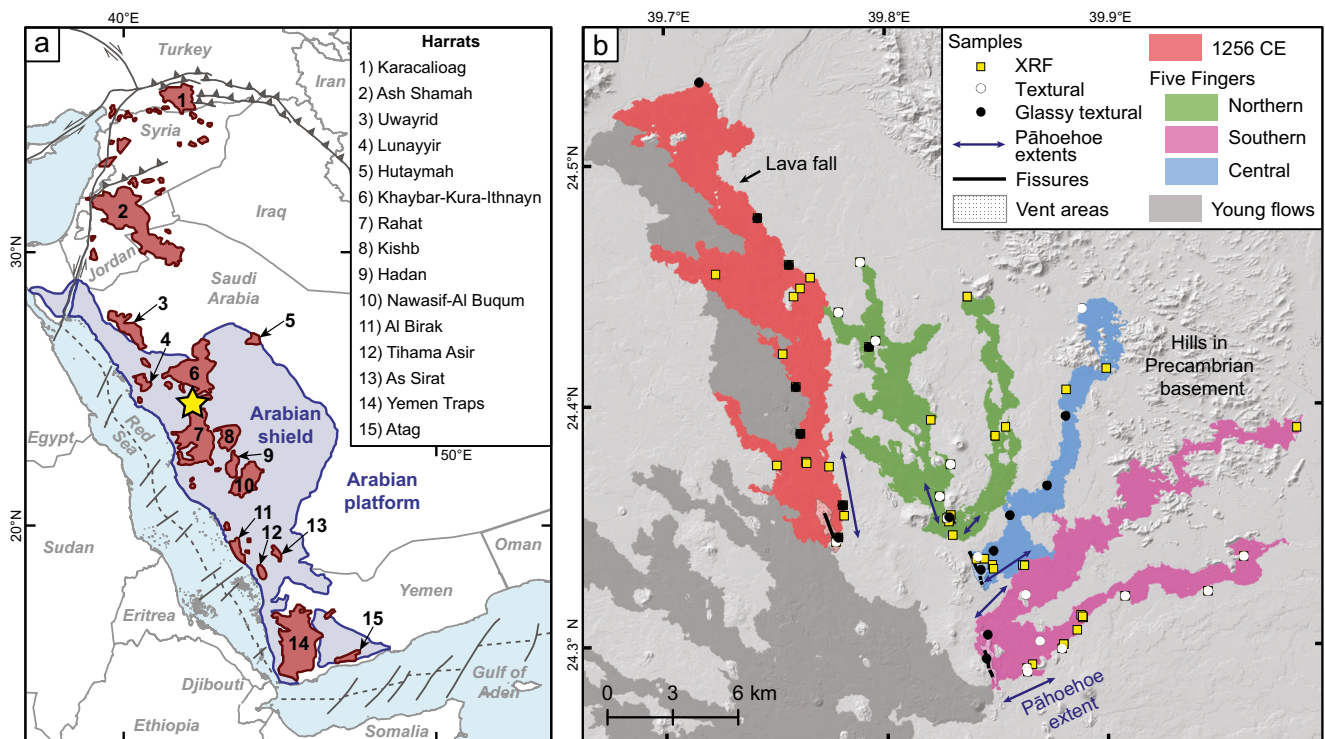
Fig. 1 **a** Location map of Harrat Rahat and other volcanic fields within the Arabian plate. The yellow star denotes the location of the study area. **b** Northeastern corner of Harrat Rahat (yellow star in **a**) showing flows of interest, morphologic features, and sample locations. Young flows are those interpreted to be < 100 ka based on appearance and morphology

morphology, and channel networks, as well as numerical modeling, have defined a series of magma pulses that fed the eruption (Camp et al. 1987; Kereson et al. 2016). Following nomenclature from Walker (1971), this eruption produced a compound lava flow field with individual lava flow units. Chemical heterogeneity within the flow field was interpreted to be driven by magma mixing and persisted through the first three eruptive pulses (Camp et al. 1987). The bulk of the flow field was emplaced during the second pulse of the eruption (pulse II) and formed the main lava flow unit with an 'a'ā channel that extends from the main vent to the north (Camp et al. 1987). Detailed mapping by Keresztori et al. (2016) shows this flow transitioning from pāhoehoe to 'a'ā at ~ 2 km from vent (Fig. 1b). Interaction with underlying topography resulted in flow ponding behind, and then eventually overtopping, a pre-existing ridge, to form a lava fall at ~ 16.5 km from the vent before stalling (Fig. 1b; Camp et al. 1987; Keresztori et al. 2016).

There are many other lava flows in northernmost Harrat Rahat that appear young, but whose ages, compositions, and emplacement conditions remain undetermined (Fig. 1b). Previous work interpreted some of those flows as Holocene (Camp and Roobol 1989, 1991; Moufti et al. 2012, 2013), but recent geochronology and paleomagnetic studies have revealed Late Pleistocene ages (Downs et al. 2018; Stelten et al. 2018). One pulse of eruptive activity during this period produced the lava flows dubbed the Five Fingers, with five branches extending 13.2–20.2 km from their vents (Fig. 1b). Based on mapped field relations, whole-rock chemistry, and phenocryst and microphenocryst characteristics, we subdivide the Five Fingers flows into the basalt of the Northern Fingers, basalt of the Central Finger, and basalt of the Southern Fingers. For simplification, these are termed the Northern, Central, and Southern flows in this paper (Fig. 1b). Past field interpretations subdivided these into only two eruptive units, and estimated their ages as post-Neolithic (Camp and Roobol 1989, 1991), although new surface exposure ages suggest a potential maximum age of 34.9 ± 3.1 ka (Murcia et al. 2017). These flows are open channel 'a'ā flows with near-vent pāhoehoe extending up to 2.5 km from vent (Fig. 1b). The Five Fingers flows can all be classified as simple after Walker (1971), although the Northern flow may be weakly compound as it has some late-stage overflows burying the main channels close to the vent (Fig. 1b). Previous work by Murcia et al. (2014) qualitatively described some of the surface morphology features and estimated volumes of these flows, but no quantitative work on flow morphology or rheology has been undertaken. Since the 1256 CE and Five Fingers lavas preserve the morphology and textures of the most recent effusive eruptions within northernmost Harrat Rahat, we focus our study on an investigation of the emplacement histories and properties of these flows.

Methods

Morphologic analysis

A sufficiently high-resolution digital elevation model (DEM) to enable quantification of morphological properties such as levee heights and channel widths is fundamental for characterizing lava flow emplacement. We utilized several elevation datasets to achieve the highest possible resolution over our study area in northernmost Harrat Rahat (Fig. 1b). Datasets included a 0.5-m-resolution lidar DEM from 2012 encompassing the 1256 CE lava flow field, provided by the Saudi Geological Survey, and a 1-m-resolution DEM of the Five Fingers area purchased from DigitalGlobe and derived from satellite photogrammetry (using DigitalGlobe WorldView-2 50-cm-resolution visible imagery from December 9, 2012 and February 7–March 6, 2014).

Flow and channel mapping

We used hillshade and slope maps derived from these DEMs to map the extents and morphology of these lava flows. The topographic data, in combination with the 50-cm-resolution WorldView-2 2012 and 2014 imagery, facilitated mapping channel margins along each flow. Channels are indistinct near the vent, where lavas are dominantly pāhoehoe, and distally, in the zone of dispersed flow and at the flow toe. We traced multiple sets of channel margins along the flows where they branched (e.g., the Northern and Southern flows within the Five Fingers).

We analyzed these flow and channel extents using cross-sections to quantify the evolution of flow and channel width down-flow after Deardorff and Cashman (2012). Cross-section lines spaced every 100 m along the channel centerline were built using the HEC-GeoRAS software (U.S. Army Corps of Engineers, http://www.hec.usace.army.mil/software/hec-georas/). To calculate channel and flow widths,

we used a geographic information system-based method from Deardorff and Cashman (2012) that buffers each cross-section line by 50 m, both up-flow and down-flow, to create measurement boxes oriented perpendicular to the flow centerline and 100 m in the flow direction (Fig. 2a). The total flow area within each box, divided by this 100-m-down-flow-distance, then represents the average flow width in this segment, whereas the narrower internal area between the channel margins is used to calculate average channel width.

Pre-eruptive topography, thickness, and volume

High-spatial-resolution morphologic analysis also allows estimation of lava flow thicknesses and volumes. This is best done by comparing pre-eruptive and post-emplacement topography to derive a flow thickness map and integrating over the flow area to calculate volume (e.g., Mazzarini et al. 2005; Coltelli et al. 2007; Soldati et al. 2018). However, since information on pre-eruptive topography is lacking, we must use the present-day topography at the flow margins to interpolate an underlying surface.

One approach is to interpolate the basal surface with a triangulated irregular network connecting points along the flow margin as was done for the 1256 CE flow field by Kereszturi et al. (2016). However, we found that this method yields regions of significant negative thicknesses for these lava flows, as Kereszturi et al. noted (2016). To avoid this, we allowed pre-eruptive elevations within the flow to be lower than the flow margins by using flow cross-sections and inserting additional points where required, similar to the method of Stevens (2002). We used the same cross-sections as for morphologic analysis, but along the full flow length, and extracted their elevations. For cross-sections where the surface of the lava flow was everywhere higher than the elevation at the margins, the base of the flow was modeled with a straight line between the end points along opposite flow edges. Where the lava flow surface was lower elevation than the margin

Fig. 2 Morphological analysis methods: an example from the southern branch of the Southern flow (see inset). a Planform morphology showing mapped flow and channel extents, flow centerline with cross-sections, and buffered cross-section boxes. b Flow thickness map constructed by subtraction of the reconstructed basal surface from present-day topography
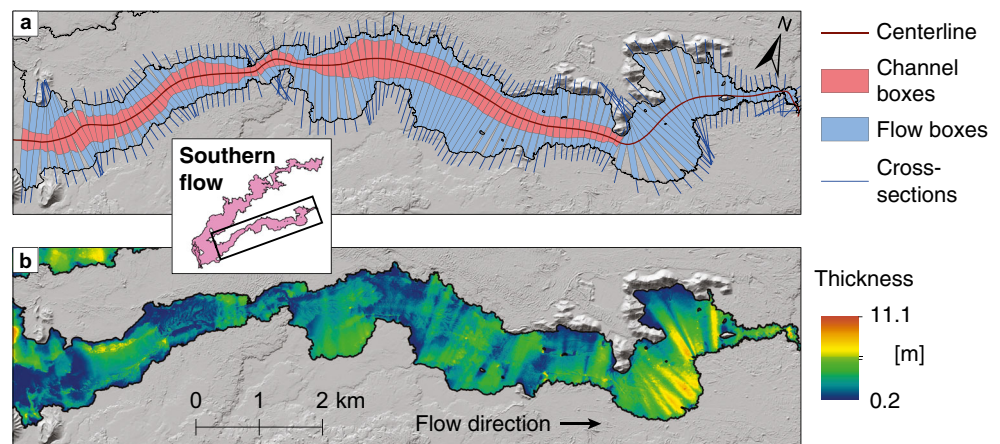
elevations, the base was defined by the minimum number of straight line segments that intersect interior low points along the cross-section, requiring a minimum thickness of 0.2 m based on our field observations (Online Resource 1). The base of the entire flow was then constructed with a natural neighbor interpolation of all of the basal cross-sections and then subtracted from the elevation of the flow top to obtain flow thicknesses and volumes (Fig. 2b). These thicknesses and volumes likely represent minimum estimates, with potential thickness underestimates on the order of a few meters where flows are strongly confined by topography. The result has artifacts from the cross-section locations, so we calculated average thicknesses within the flow boxes to smooth the results and for comparison with other morphology metrics.

Finally, we measured the slope of the channel surface and the entire flow, as well as its interpolated base, using the same cross-section boxes. The averaged slopes of the flow-top segments were calculated after Deardorff and Cashman (2012) by fitting a planar surface to the portion of the DEM within the lava channel in each box and extracting its topographic gradient. Test datasets were also made using the interpolated flow base from the thickness calculations and the full flow area, instead of the channel. However, the slope of the interpolated base and the full flow area were much noisier than the slope extracted from within the channel, with artifacts from the cross-section spacing in the interpolated surface and disruption from the morphology of the levees and overflows within the full area of the flow. We therefore used the present-day channel surface to calculate the slope, which succeeds in capturing changes in slope such as the lava fall in the 1256 CE flow (Fig. 3b), but is limited to the channel extent and is only a best approximation of the pre-eruptive slope.

Geochemical and textural analysis

To characterize the bulk compositions of the 1256 CE and Five Fingers eruptive products, we collected and analyzed 37 scoria and lava samples from throughout these units (squares in Fig. 1b; Table 1; locations in Online Resource 2). Major-oxide analyses were performed by X-ray fluorescence at the GeoAnalytical Laboratory at Washington State University (USA).

Another set of 35 samples were collected for textural analysis down-flow from vent to toe at flow levees with an effort to select samples that preserve original air-quenched textures, including near-vent tephra (circles in Fig. 1b; locations in Online Resource 2; sampling methods after, e.g., Crisp et al. 1994; Riker et al. 2009; Robert et al. 2014). Despite field selection of glassy samples, thin section analysis revealed that only 16 samples preserved significant glass appropriate for textural and chemical analyses (black circles in Fig. 1b). We restricted our geochemical and textural interpretations to the glassy margins of these samples.

We used a JEOL JXA-8900 wavelength-dispersive electron microprobe to measure the chemistry of minerals and glass as a record of the syn-eruptive state of the lava. We used a 15-kV accelerating voltage for all analyses and a current of 5 nA and a 5-μm spot size for glass, a current of 10 nA and a 5-μm spot size for plagioclase microphenocrysts, and applied 30 nA with a focused beam for olivine microphenocrysts.

Textural data were derived from scanning electron microscope (SEM) backscattered electron images at a range of magnifications (×10–800, 10–30 images per sample). We mosaicked images and post-processed these with threshold ranges to make each phase a uniform grayscale color (after Shea et al. 2010). Post-processed images were analyzed with ImageJ to calculate phase proportions and crystal shapes. We measured crystal aspect ratios only for crystals with areas larger than 10^{-5} mm^2 to reduce the influence of pixel-scale noise, and we corrected for stereological effects after Higgins (2000).

Characterization of lava temperature, viscosity, and effusion rate

To reconstruct eruptive conditions, we first independently characterized flow viscosity petrologically and then combined these viscosities with the morphology metrics to assess effusion rates. We calculated lava viscosity as a function of the liquid viscosity and the effects of crystallinity and vesicularity (methods after Llewellin and Manga 2005; Costa 2005; Giordano et al. 2008; Costa et al. 2009; Mueller et al. 2011; Mader et al. 2013). Effusion rates were then estimated from these viscosities, as well as channel width and topographic slope, using a model of channel formation in solidifying viscous flows from analytical theory and experiments by Kerr et al. (2006).

Geothermometry

Lava viscosity is strongly controlled by its temperature and this can be calculated from the compositions of coexisting mineral phases (e.g., Shaw 1972; Crisp et al. 1994; Giordano et al. 2008; Putirka 2008). We applied a suite of geothermometers based on liquid chemistry, olivine-liquid equilibrium, and plagioclase-liquid equilibrium from Helz and Thornber (1987), Beattie (1993), Sisson and Grove (1993), Montierth et al. (1995), Putirka et al. (2007), and Putirka (2008). Each geothermometer assumes that phases are in equilibrium and some use estimates of dissolved water content and pressure (see Putirka 2008 for a review). We used VolatileCalc (Newman and Lowenstern 2002) to model water content at atmospheric pressure and measured glass SiO$_2$ concentrations.
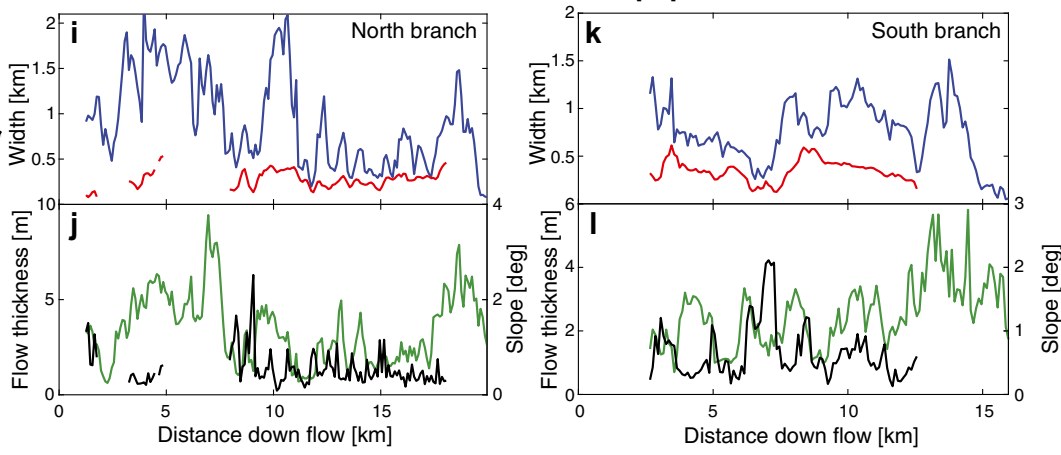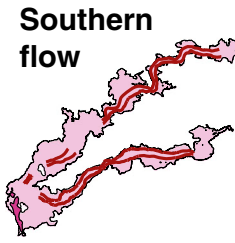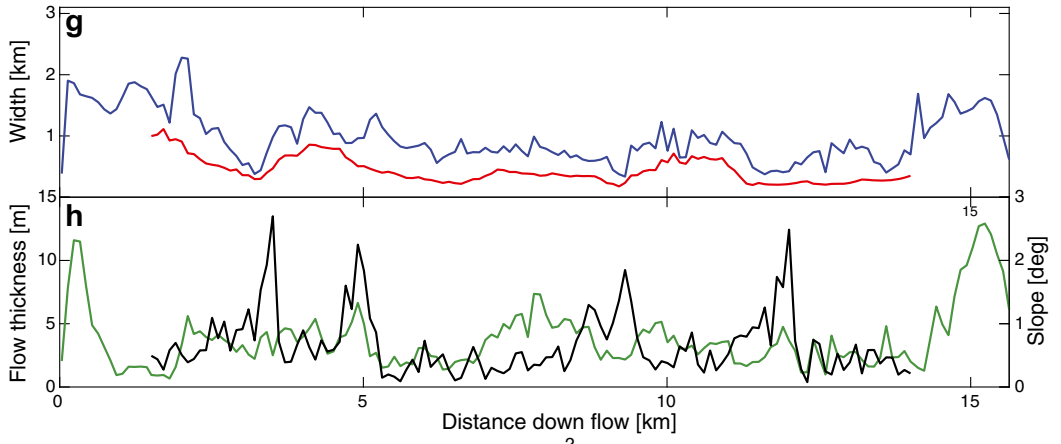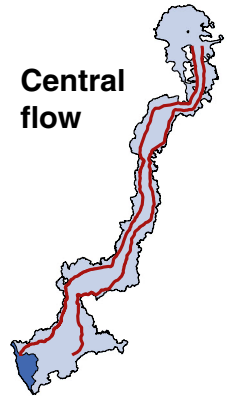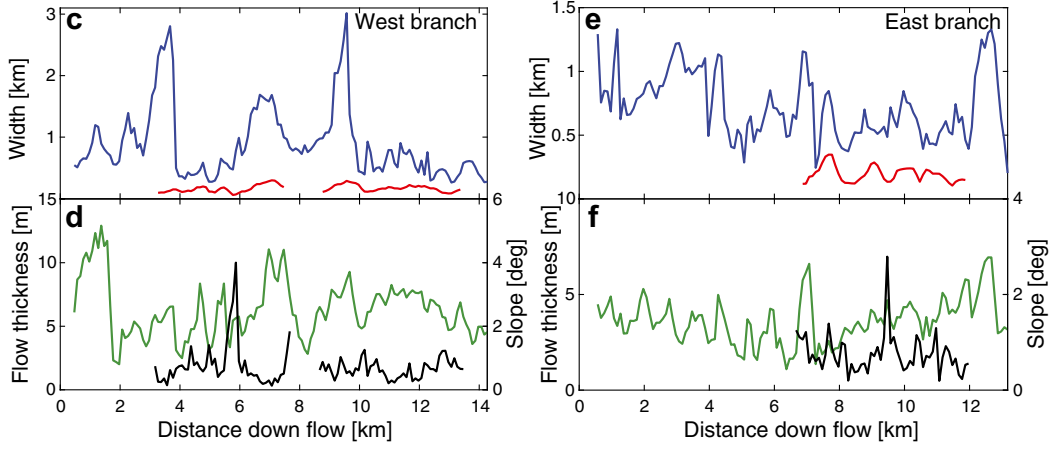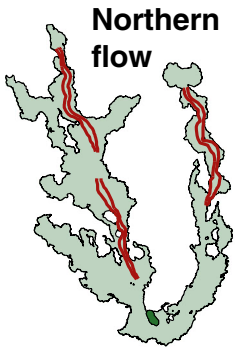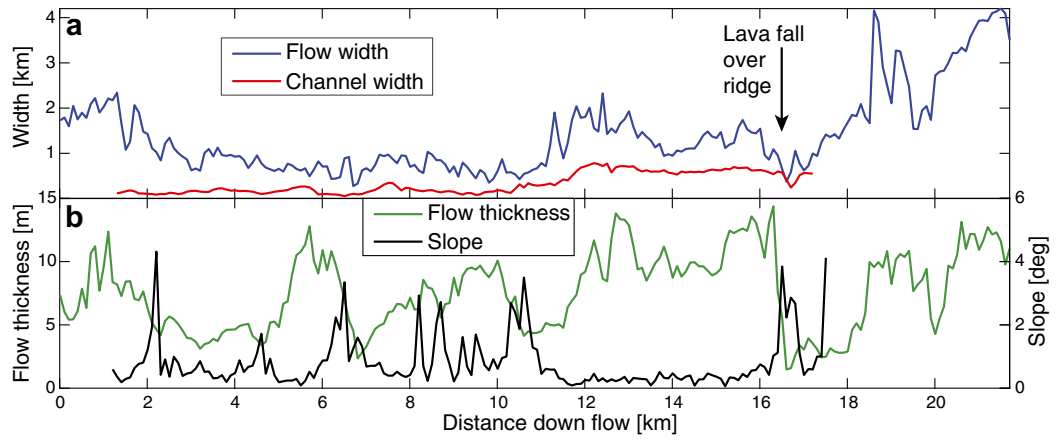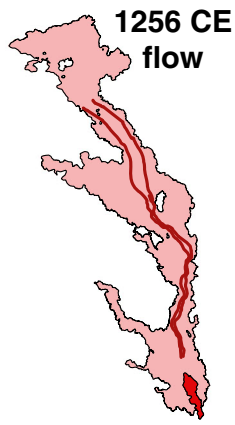
◀ **Fig. 3** Overview of morphometric data derived along each flow. Flow width (blue) and channel width (red) are shown in the upper plots (**a, c, e, g, i, k**), while flow thickness (green) and slope (black) are shown in the lower plots (**b, d, f, h, j, l**). Channel width and slope are only calculated where the channel is well-defined (Fig. 2). Mapped levees are shown as red lines in the flow maps on the left margin

Viscosity

The viscosity of the bulk lava is influenced by the viscosity of the liquid phase, as well as its crystallinity and vesicularity (e.g., Llewellin and Manga 2005; Giordano et al. 2008; Costa et al. 2009; Mueller et al. 2011; Mader et al. 2013). To calculate the mixture viscosity, we computed the liquid viscosity, added the relative effect of crystals on the bulk viscosity, and then assessed the impact of the vesicle fraction.

We model the apparent bulk viscosity (η_{app}) of our samples as a function of the viscosity of the residual liquid (η_{liq}) and the relative viscosity based on the crystal or vesicle content (η_r):

$$\eta_{app} = \eta_{liq}\eta_r. \tag{1}$$

We calculated liquid viscosity (η_{liq}) from glass compositions and calculated temperatures using the model of Giordano et al. (2008). Viscosity is highly sensitive to H_2O dissolved in the melt, and we applied our water content estimates at atmospheric pressure from VolatileCalc based on the glass compositions (Newman and Lowenstern 2002).

The relative viscosity (η_r) can be estimated from a variety of different models to account for the effects of the solid fraction. Crystallinities were adjusted for analysis to exclude the volume fraction of bubbles by normalizing the crystal fraction to the vesicle-free (melt + crystals) fraction (e.g., Mader et al. 2013; Robert et al. 2014; Soldati et al. 2018). In the first model, from Mueller et al. (2011), all particles are treated as identical and have the shape of the observed crystals. Elongate particles reduce the effective maximum packing volume fraction of the particles (ϕ_m) following a relationship derived experimentally by Mueller et al. (2011):

$$\phi_m = \phi_{m_1} exp\left[-\frac{(\log_{10}r_p)^2}{2b^2}\right], \tag{2}$$

where r_p is the crystal aspect ratio, ϕ_{m_1} is the maximum packing fraction for particles with $r_p = 1$, and b is the variance of the log-Gaussian function. We used the observed crystal aspect ratio and the best-fit values of ϕ_{m_1} and b for natural crystals (Mader et al. 2013) to calculate the maximum packing fraction (ϕ_m). As the crystallinity (ϕ) increases with cooling, and approaches this value, the

relative viscosity (η_r) will rise rapidly following Maron and Pierce (1956):

$$\eta_r = \left(1 - \frac{\phi}{\phi_m}\right)^2. \tag{3}$$

This model can describe the evolution in apparent viscosity at low crystal fraction, but becomes infinite at the maximum packing fraction, whereas lavas are still capable of deformation at higher crystal contents (e.g., Costa 2005; Mader et al. 2013; Bergantz et al. 2017).

We therefore extend our analysis using a second model from Costa (2005) and Costa et al. (2009) that seeks to capture behavior at any crystal fraction. This model determines relative viscosity as a function of strain rate because the rheology of crystal-rich flows is likely non-Newtonian (Castruccio et al. 2014). Although parameters for the model must be determined experimentally, we use values from Cimarelli et al. (2011) that best reflect the Harrat Rahat crystal aspect ratio (r_p). We calculate values for two different strain rates (10^{-4} and 1 s^{-1}).

We also estimated the effect of the vesicle fraction following Llewellin and Manga (2005) and Mader et al. (2013) to account for the addition of vesicles to the melt + crystals mixture. The modeled effect of the vesicle fraction varies with strain rate and vesicle size, so we test two different strain rates (10^{-4} and 1 s^{-1}) and use an average bubble radius of 0.01 mm following Llewellin and Manga (2005) and Mader et al. (2013).

Estimation of effusion rates

Analytical theory, analogue experiments, and observations of eruptions suggest that lava channel geometry is controlled by effusion rate, underlying slope, and flow rheology (e.g., Hulme 1974; Harris and Rowland 2001; Kerr et al. 2006). In flows that are cooling and growing a surface crust, crustal growth and lateral flow spreading will balance at a given volumetric flux, viscosity, and slope to develop a channel of constant width (Kerr et al. 2006). Following Kerr et al. (2006), the relationship between parameters can be written as an equation for flow width, w,

$$w = 2\left[\frac{(g\Delta\rho)^2 Q^7 \eta^4 \cos^9\theta}{\sigma_c^6 \kappa^3 \sin^7\theta}\right]^{1/13}, \tag{4}$$

where g is gravity, $\Delta\rho$ is density of the flow relative to its environment, Q is volumetric flux through the channel, η is viscosity, θ is slope, σ_c is crustal yield strength, and κ is thermal diffusivity. We use a value of 2400 kg m^{-3} for bulk flow density for these low-vesicularity basalts (Shea et al. 2010; Downs et al. 2018). Values for σ_c range from 10^4 to 10^6 Pa, while a value of 10^{-6} m^2 s^{-1} for κ is mostly commonly used for basalt (Blake and Bruno 2000; Kerr et al. 2006; Kerr and Lyman 2007; Deardorff and Cashman 2012; Cashman et al.

Table 1   Representative whole-rock chemical analyses of the 1256 CE and Five Fingers eruptions

Unit name	SiO_2	TiO_2	Al_2O_3	FeO*	MnO	MgO	CaO	Na_2O	K_2O	P_2O_5	LOI	Total
1256 CE flow												
R14AC056	46.90	2.97	16.00	12.66	0.22	6.35	8.80	4.19	0.95	0.97	0.00	99.11
R15DD150A	46.81	1.83	16.24	11.36	0.18	8.98	11.31	2.76	0.32	0.20	0.00	98.96
R14TS012	46.77	3.00	16.07	12.98	0.22	6.05	8.67	4.23	0.97	1.02	0.00	99.70
R14TS093	46.68	3.00	16.02	13.12	0.22	6.02	8.60	4.31	0.99	1.05	0.00	99.81
R14TS096	46.84	3.02	16.10	12.84	0.22	5.95	8.73	4.26	0.99	1.05	0.00	99.65
R14TS097	47.01	3.01	16.27	12.96	0.22	5.93	8.46	4.12	0.99	1.03	0.00	99.63
R14TS098	46.51	2.10	16.03	11.49	0.18	9.47	10.48	3.00	0.43	0.30	0.00	99.19
R14TS100	46.86	3.07	16.17	12.85	0.22	5.96	8.54	4.26	1.00	1.06	0.00	99.48
R14TS102	47.03	3.05	16.19	13.03	0.22	6.00	8.35	4.19	0.98	0.94	0.00	99.43
R14TS103	46.86	3.02	16.10	12.86	0.22	6.03	8.59	4.26	0.99	1.05	0.00	99.91
R14TS104	46.74	3.04	16.02	13.09	0.22	6.01	8.50	4.28	1.02	1.08	0.00	99.53
R14TS142	46.57	1.99	16.67	11.55	0.18	8.64	10.75	3.02	0.38	0.24	0.00	99.97
Northern flow												
R15DD011	45.87	3.68	16.44	13.06	0.19	6.49	9.49	3.55	0.82	0.40	0.00	99.68
R15DD018	45.75	3.46	15.95	12.80	0.19	7.40	9.80	3.45	0.82	0.39	0.98	98.42
R14DS079	45.80	3.61	16.25	12.97	0.19	6.88	9.25	3.81	0.84	0.40	0.00	99.08
R14DS082	45.77	3.64	16.35	12.96	0.19	6.79	9.27	3.83	0.81	0.39	0.00	99.57
R15DS097	45.92	3.74	16.51	13.22	0.21	6.58	9.04	3.53	0.81	0.44	0.00	99.08
R15DS099	45.91	3.63	16.41	12.90	0.19	6.78	9.39	3.61	0.78	0.40	0.00	100.04
R15DS100	45.78	3.64	16.42	13.22	0.20	6.52	9.33	3.65	0.83	0.41	0.00	99.76
R14TS017	45.26	3.65	16.30	13.20	0.19	6.58	9.67	3.93	0.82	0.40	0.87	98.38
R14TS019	45.89	3.72	16.50	13.38	0.20	6.73	8.77	3.57	0.81	0.41	0.00	99.04
R14TS020	45.89	3.68	16.47	13.22	0.19	6.66	9.12	3.56	0.81	0.39	0.00	98.79
Central flow												
R14AC008	45.82	3.44	16.02	13.21	0.19	7.61	9.07	3.58	0.75	0.32	0.00	99.99
R14AC009	45.30	3.48	15.80	13.21	0.18	7.51	9.73	3.69	0.77	0.33	0.00	98.87
R14TS011	45.42	3.63	16.27	13.20	0.22	6.94	9.39	3.55	0.82	0.56	0.24	98.71
R14TS024	45.82	3.65	16.25	13.28	0.20	7.14	8.92	3.54	0.79	0.42	0.00	99.24
R16MS071	45.92	3.65	16.26	13.17	0.19	6.81	9.13	3.61	0.87	0.39	0.00	99.39
Southern flow												
R14AC005	46.18	2.36	15.72	12.04	0.18	8.88	11.05	2.93	0.43	0.24	0.00	98.92
R14AC006	45.98	2.35	15.86	12.04	0.18	8.57	11.40	2.95	0.44	0.23	0.03	99.64
R14AC007	46.09	2.49	15.86	12.28	0.18	8.82	10.60	2.96	0.47	0.26	0.00	99.81
R15DD019	46.03	2.32	15.88	11.80	0.19	8.92	11.36	2.77	0.45	0.26	0.46	99.64
R15DD022	46.19	2.36	16.10	11.90	0.18	8.79	11.09	2.76	0.38	0.24	0.00	99.56
R15DD025	46.21	2.30	15.66	11.49	0.18	8.64	12.08	2.76	0.44	0.24	0.91	98.71
R15DS101	46.56	2.36	15.81	11.92	0.18	8.97	10.61	2.92	0.44	0.22	0.00	98.57
R15DS105	46.18	2.34	15.85	12.19	0.18	8.75	11.04	2.81	0.43	0.24	0.00	99.38
R14TS008	46.01	2.34	15.72	12.22	0.18	8.93	11.16	2.77	0.43	0.24	0.00	99.41
R14TS026	46.06	2.48	16.20	11.64	0.21	8.48	11.21	2.84	0.53	0.36	0.81	98.96

Note: Major-oxide (as weight %) analyses were performed by X-ray fluorescence. Values have been recalculated to 100% anhydrous, but original loss on ignition (LOI) and totals are given

2013; Castruccio et al. 2013). The volumetric flux of lava through the channel derived from this equation provides an estimate of the average local effusion rate through the whole channel while it was active.

The crustal yield strength is typically calculated by fitting this model to flow advance data (Blake and Bruno

2000; Kerr et al. 2006; Kerr and Lyman 2007; Castruccio et al. 2013); however, we lack such observations for these eruptions. We therefore calculate a best-fit value for σ_c for the Harrat Rahat basalts by fitting Eq. 4 to parameters for the 1256 CE eruption, which is the only eruption for which we have an independent estimate of effusion rate from the observed total mean output rate of the eruption (total volume/total duration). This assumes that the channel morphology represents flow at the average local effusion rate through the channel during the eruption (Eq. 4). Instantaneous effusion rates would be higher or lower as the eruption waxed and waned, but using the constraint of the total mean output rate offers an educated, if uncertain, estimate for this parameter for the 1256 CE flow.

We adopt this crust-dominated model for flow emplacement and channelization to estimate the effusion rates that formed the observed 'a'ā channel morphology after Kerr et al. (2006) and Deardorff and Cashman (2012). This regime assumes a flow with a core viscosity, retarded by a growing surface crust, rather than an evolving bulk rheology. We lack flow advance data to fully test for crust-dominated behavior or discard alternatives, but analyses of similar flows in the literature support the application of this model (e.g., Kilburn and Lopes 1991; Kerr et al. 2006; Lyman and Kerr 2006; Castruccio et al. 2013). We therefore use our calculations of apparent viscosity to constrain the core viscosity, averaging apparent viscosities in log space to capture values with intermediate crystallinity and temperature. We exclude samples with crystallinities greater than the maximum packing fraction in our averages because they are unlikely to represent the insulated flow interior beneath the surface crust. Using the method of Deardorff and Cashman (2012), we combine these core viscosities with the slope and width measurements from morphologic analysis to fit Eq. 4 to our data and calculate the best-fit volumetric flux through each channel. The results

represent the best-fit local effusion rate during channelized flow, which we use as an approximation of the average effusion rate for the emplacement of each flow branch.

Results

Whole-rock geochemistry

Whole-rock major-oxide compositions are summarized in Table 1. Our data show that the 1256 CE eruption produced both alkalic and tholeiitic compositions, as well as hybrid compositions interpreted as the result of mixing of these end-member compositions. A similar conclusion was reached by Camp et al. (1987). The Five Fingers lavas all consist of alkalic basalt typical of Harrat Rahat volcanism, but each of the three eruptions that make up the Five Fingers are compositionally distinct.

Morphologic analysis

Morphology measurements are summarized for all flows and branches in Fig. 3 and Table 2. Field contacts allow us to distinguish the boundaries between the Five Fingers flows. The Central flow was the first of the Five Fingers to erupt based on stratigraphic relations, but it is unknown if the Northern or the Southern flows erupted second, as their lava flows are not in contact. The channel networks are mostly simple, with each branch containing a single channel. Where levees are well-defined, they stand 1–6 m above the channel, but it is not possible to trace the levees along the entire flow length due to burial by proximal pāhoehoe and later overflows (cf. Robert et al. 2014). No channels are present within the zone of dispersed flow near the flow toes. Distally, the Central flow and the northern branch of the Southern flow advanced

Table 2 Flow and channel morphology results

Flow	Vent volume (km³)	Flow volume (km³)	Total volume DRE (km³)	Flow length (km)	Mean flow thickness (m)	Mean flow width (m)	Mean channel width (m)	Mean slope (deg)
1256 CE flow	0.02	0.44	0.42	21.8	7.7 ± 0.2	1403 ± 61	329 ± 18	0.80 ± 0.06
Northern flow	0.01	0.18	0.17	14.3				
West branch		0.14		14.3	6.3 ± 0.2	888 ± 49	165 ± 6	0.72 ± 0.06
East branch		0.04		13.2	3.6 ± 0.1	728 ± 23	194 ± 9	0.75 ± 0.06
Central flow	0.01	0.07	0.07	15.7	3.8 ± 0.2	978 ± 34	436 ± 19	0.67 ± 0.04
Southern flow	0.01	0.14	0.13	20.2				
North branch		0.09		20.2	3.43 ± 0.1	924 ± 38	276 ± 8	0.54 ± 0.03
South branch		0.05		16.6	2. ± 0.1	791 ± 26	346 ± 11	0.65 ± 0.04

DRE volume calculated using 2600 kg m⁻³ for dense rock, 2400 kg m⁻³ for lava, and 1500 kg m⁻³ for tephra. Volume estimates are likely minimums due to the lack of pre-eruptive topography. Flow lengths are measured along the main channel from vent to toe. Errors are standard errors. The full range of values is shown in Fig. 3

through hills of Precambrian basement to the east, becoming confined in narrow valleys (Fig. 1b, Camp and Roobol 1989). The 1256 CE flow has a more complex branched network (Kereszturi et al. 2016), and for channel and flow morphology metrics we extracted only the main channel from pulse II of the eruption, which was by far the largest in volume and extends from near-vent to toe (Fig. 3a, b; Camp et al. 1987). The flows vary in size considerably, with minimum bulk flow volumes ranging from 0.07 km^3 for the Central flow to 0.44 km^3 for the 1256 CE flow (Table 2). As expected, flow thickness and slope show an inverse relationship (cf. Walker 1973). There is evidence of flow thickening upslope of large slope increases, particularly in the 1256 CE flow field at ~ 16 km down-flow where the lava ponded above the lava fall at ~ 16.5 km identified by Camp et al. (1987; Fig. 1b and 3b).

Petrologic analysis

Major-oxide glass and mineral compositions averaged for each sample are presented in Table 3 with complete results in Online Resource 2. Variations in composition across the flow fields show glass SiO$_2$ ranging from 44 to 49 wt%, plagioclase spanning An$_{56-71}$, and olivine with Fo$_{67-83}$. Glass Al$_2$O$_3$ and MgO both decrease slightly with distance down-flow, while K$_2$O increases, consistent with crystallization with emplacement time and cooling away from the vent. A single sample (R15DD150B) of tholeiitic composition from 1256 CE was analyzed and, as expected, had crystals with higher An and Fo contents than other 1256 CE samples. The lack of quenched samples from the Northern and Southern flows prevents detailed analysis of their down-flow evolution. We therefore use available data to provide estimates of the textural and rheological parameters for these flows, but only make interpretations of down-flow changes based on the flows with more complete datasets (i.e., for the 1256 CE and Central flow fields).

Textural analysis yields variations in crystallinity and vesicularity. Proportions of crystals from image analysis show crystallinity increasing down-flow. Analysis of vesicles reveals high vesicularity for tephra and spatter (32% on average), and low vesicularity for lava samples (6% on average; Fig. 4). Plagioclase dominates the crystal fraction, but we identify olivine and oxides in nearly all samples (Table 4). We assign an uncertainty of 2% to these phase proportions to account for textural variability within the samples based on analysis of sub-samples of images. Crystals with areas greater than 10^{-5} mm^2 are euhedral and have broad-peaked distributions in aspect ratio in 2D intersection, indicative of 3D aspect ratios of ~ 3.5 for plagioclase and ~ 2 for olivine (Higgins 2000). A majority of samples contain sparse (< 1%) resorbed phenocrysts of 0.5–2 mm plagioclase and olivine.

Analysis of emplacement conditions

Thermometry

We average results from all of the individual geothermometers to derive lava temperatures for each sample (Table 4; full results given in Online Resource 2). Calculated dissolved H$_2$O concentrations used for geothermometry were 0.08–0.09 wt% H$_2$O based on glass compositions at 1 bar (Newman and Lowenstern 2002), consistent with the high microprobe totals for glass analyses (Table 3). Our results capture near-vent temperatures for the flows of 1120–1150 °C (Table 4). Results from the 1256 CE and Central flows show an overall cooling trend with distance from vent (Fig. 5), with lava temperatures dropping from ~ 1140 to ~ 1090 °C over 9–20 km, giving cooling rates of 2–7 °C km^{-2}. These trends are also supported by the more limited data from the Northern and Southern flows (Fig. 5). Although the 1256 CE flow is chemically diverse (Tables 1 and 3), the only tholeiitic sample analyzed (R15DD150B) shows temperatures within the same range as the alkalic samples (~ 1139 ± 6 °C).

Viscosity

Melt viscosities calculated with the model from Giordano et al. (2008) increase with cooling down-flow, and range from 10^2 to 10^3 Pa s (Table 4). To add the effect of the crystal fraction after Mueller et al. (2011), the average Harrat Rahat crystal aspect ratio (r_p) of 2.7 yields a maximum packing fraction (ϕ_m) of 0.50 from Eq. 2. Integrating results from Eqs. 1–3, the apparent viscosities of the Harrat Rahat lavas are on the order of 10^2–10^3 Pa s and increase by nearly 3 orders of magnitude with distance down-flow for the well-sampled 1256 CE flow (Fig. 6, solid lines; Table 4).

Viscosities at higher crystal fractions are derived from the model of Costa (2005) and Costa et al. (2009). Using experimentally derived parameters from Cimarelli et al. (2011) that best match the Harrat Rahat crystal aspect ratio (Type C in their paper with $r_p = 1.82$), results follow the Mueller et al. (2011) dilute mixture model until the crystallinity reaches maximum packing (Fig. 6; Table 4). Lower values at the higher strain rate demonstrate that the flow is undergoing shear thinning at very high crystallinities (Mader et al. 2013), but the effect of strain rate on apparent viscosity is small relative to changes in temperature and crystallinity. Viscosities range from 10^2 to 10^9 Pa s with vesicle-free crystallinities between 1 and 65% (Table 4). Although the 1256 CE and Central flows show viscosity increasing with distance from vent (Fig. 6), sampling of the Northern and Southern flows is not complete enough to show confident trends.

Table 3 Microprobe analysis of glass, plagioclase, and olivine compositions

	1256 CE flow						Northern flow	
Sample	R14TS95	R15DD150B	R15DD015	R15DD012	R15DD010	R16HD010	R15DD18	R15DD14
Description	Tephra	Lava	Lava	Lava	Lava	Lava	Spatter	Lava
Distance from vent (km)	0	3.8	6.0	12.0	14.3	22.0	0	8.9
Glass								
SiO_2	47.2	46.4	45.7	45.6	47.2	47.7	47.6	46.2
TiO_2	3.13	3.74	4.10	3.94	3.75	4.56	5.21	5.01
Al_2O_3	16.3	14.8	14.8	14.9	15.9	14.2	14.4	15.4
FeO	13.0	13.6	13.7	14.1	14.2	15.2	14.9	14.8
MnO	0.21	0.28	0.31	0.26	0.28	0.27	0.27	0.24
MgO	5.30	5.48	3.93	4.46	4.98	3.49	4.60	4.75
CaO	8.50	9.91	9.00	8.48	8.71	10.27	7.75	8.70
Na_2O	4.32	3.96	4.25	3.90	3.85	4.01	3.01	3.67
K_2O	0.99	0.82	1.77	1.37	1.33	1.72	1.28	1.07
Cl	–	0.02	0.03	0.03	0.02	0.04	0.02	0.03
P_2O_5	1.11	0.60	1.70	1.67	1.25	1.12	0.71	0.67
Total	100.1	99.5	99.3	98.7	101.6	102.6	99.7	100.7
N	51	11	15	15	15	5	13	9
Plagioclase								
SiO_2	53.1	50.3	53.7	53.4	52.7	51.4	52.0	52.8
TiO_2	–	0.17	0.20	0.21	0.17	0.25	0.19	0.22
Al_2O_3	28.6	30.0	28.1	27.9	29.4	29.8	29.7	29.0
FeO	1.14	0.83	0.73	0.81	0.74	0.90	0.72	0.69
MnO	–	0.05	0.04	0.05	0.07	0.08	0.02	0.05
MgO	0.26	0.36	0.10	0.15	0.13	0.25	0.13	0.11
CaO	12.1	14.3	11.6	11.8	12.8	13.7	12.9	13.0
Na_2O	4.67	3.15	4.69	4.56	4.20	3.74	4.08	4.24
K_2O	0.27	0.10	0.26	0.27	0.21	0.18	0.20	0.19
BaO	–	0.05	0.04	0.03	0.05	0.08	0.09	0.05
SrO	–	0.07	0.22	0.11	0.17	0.19	0.14	0.19
Total	100.1	99.3	99.7	99.3	100.6	100.6	100.2	100.5
An	57.9	71.1	56.9	57.9	62.0	66.3	62.9	62.1
Ab	40.5	28.3	41.6	40.6	36.8	32.7	36.0	36.8
Or	1.55	0.59	1.54	1.56	1.18	1.01	1.17	1.09
N	21	7	15	15	15	15	10	6
Olivine								
SiO_2	37.6	38.9	37.2	37.3	38.0	37.8	37.6	38.5
TiO_2	–	0.04	0.09	0.12	0.07	0.07	0.15	0.11
Al_2O_3	–	0.15	0.07	0.06	0.05	0.06	0.05	0.06
FeO	24.2	15.7	27.2	26.9	24.9	25.2	24.6	23.5
MnO	0.41	0.26	0.54	0.52	0.46	0.47	0.39	0.39
MgO	37.0	43.0	34.7	35.0	36.9	37.0	36.4	37.7
CaO	0.37	0.39	0.35	0.39	0.45	0.44	0.14	0.33
Na_2O	–	0.04	0.06	0.06	0.03	0.05	0.04	0.04
K_2O	–	0.00	–	–	–	–	0.00	0.03
Cr_2O_3	–	0.03	0.04	0.02	0.01	0.03	0.03	0.06
NiO	0.08	0.15	0.01	0.01	0.02	0.01	0.08	0.07

Table 3 (continued)

Total	99.6	98.7	100.2	100.4	100.8	101.0	99.5	100.9
Fo	72.8	82.8	69.0	69.5	72.2	72.0	72.2	73.7
Fa	26.7	16.9	30.3	29.9	27.3	27.5	27.4	25.8
Tp	0.46	0.28	0.62	0.58	0.51	0.52	0.44	0.43
N	8	9	25	23	30	19	4	10

	Central flow					Southern flow		
Sample	R16HD01	R16HD14	R16HD13	R16HD15	R16HD16	R16HD09	R16HD27	R16HD26
Description	Spatter	Lava	Lava	Lava	Lava	Spatter	Spatter	Lava
Distance from vent (km)	0	1.0	3.0	5.2	8.8	0	0	0.3
Glass								
SiO_2	46.9	44.7	44.3	52.0	48.9	47.2	46.4	47.3
TiO_2	4.40	4.68	4.93	4.58	5.45	3.69	3.72	5.03
Al_2O_3	16.4	12.1	11.9	13.9	12.9	15.5	14.7	12.6
FeO	13.2	14.5	16.4	10.2	11.9	13.8	13.5	13.6
MnO	0.19	0.32	0.32	0.26	0.28	0.27	0.29	0.33
MgO	5.41	5.00	4.71	2.92	3.35	6.01	5.49	3.86
CaO	8.29	11.11	10.14	7.22	8.40	10.28	9.96	12.32
Na_2O	4.15	3.21	3.28	3.89	3.75	3.31	3.99	3.72
K_2O	0.90	1.59	1.71	2.38	2.56	0.69	0.82	1.28
Cl	0.03	0.02	0.02	0.04	0.04	0.02	0.02	0.02
P_2O_5	0.56	0.66	0.66	1.11	1.34	0.58	0.60	0.83
Total	100.4	97.9	98.4	98.5	98.9	101.3	99.5	100.9
N	15	13	11	11	9	15	15	12
Plagioclase								
SiO_2	52.4	52.7	50.9	53.2	53.6	51.1	51.7	52.8
TiO_2	0.29	0.25	0.17	0.22	0.29	0.16	0.12	0.23
Al_2O_3	29.4	29.2	30.1	29.0	28.2	30.9	29.8	29.4
FeO	0.77	0.78	0.78	0.95	1.04	0.67	0.70	0.68
MnO	0.05	0.04	0.03	0.04	0.02	0.05	0.07	0.06
MgO	0.12	0.10	0.14	0.17	0.17	0.17	0.14	0.24
CaO	12.8	12.5	13.2	12.3	11.8	14.0	13.5	13.2
Na_2O	4.21	4.25	3.74	4.32	4.59	3.55	3.64	3.95
K_2O	0.21	0.20	0.15	0.23	0.29	0.13	0.14	0.17
BaO	0.07	0.10	0.04	0.10	0.04	0.07	0.10	0.11
SrO	0.25	0.20	0.16	0.16	0.23	0.13	0.13	0.28
Total	100.6	100.3	99.4	100.7	100.3	100.9	100.0	101.1
An	62.0	61.2	65.6	60.3	57.8	68.0	66.7	64.2
Ab	36.8	37.6	33.5	38.3	40.5	31.3	32.5	34.8
Or	1.19	1.19	0.88	1.34	1.67	0.75	0.82	0.98
N	10	8	10	5	11	11	7	9
Olivine								
SiO_2	38.0	38.7	37.0	38.1	37.4	38.8	38.8	38.5
TiO_2	0.10	0.09	0.06	0.09	0.15	0.05	0.08	0.14
Al_2O_3	0.08	0.06	0.05	0.06	0.10	0.07	0.06	0.14
FeO	22.6	21.1	29.0	22.5	26.1	19.4	19.8	21.6
MnO	0.37	0.30	0.61	0.38	0.51	0.28	0.33	0.37

Table 3 (continued)

MgO	38.8	40.2	33.8	39.0	41.7	35.5	40.7	39.1
CaO	0.32	0.24	0.34	0.31	0.37	0.53	0.32	0.48
Na_2O	0.04	0.02	0.06	0.03	0.05	0.05	0.03	0.06
K_2O	0.02	0.02	0.02	0.02	0.02	0.01	0.02	0.03
Cr_2O_3	0.06	0.09	0.06	0.05	0.08	0.02	0.07	0.06
NiO	0.08	0.10	0.06	0.08	0.14	0.10	0.11	0.10
Total	100.6	100.9	101.0	100.6	101.0	100.4	100.2	100.6
Fo	75.0	77.0	67.1	75.3	79.0	70.4	78.3	76.0
Fa	24.5	22.7	32.3	24.3	20.7	29.0	21.3	23.6
Tp	0.41	0.32	0.69	0.41	0.30	0.57	0.36	0.41
N	13	6	12	12	15	12	5	4

Note: These values are sample averages. Rows labeled "N" show the number of samples analyzed for each phase in each sample. See Online Resource 2 for all measurements. We use a JEOL JXA-8900 wavelength-dispersive electron microprobe to measure the chemistry of minerals and glass. The instrument was standardized on a selection of natural and synthetic glasses and minerals, and background-corrected X-ray count rates were converted to oxide concentrations with the JEOL proprietary version of the CITZAF reduction scheme (Armstrong JT, 1995, CITZAF: a package of correction programs for quantitative electron microbeam X-ray analysis of thick polished materials, thin films, and particles. Microbeam Anal 4:177–200)

Since these flows generally have low vesicularity away from their vents (the average vesicularity for all lava samples is 5.8%, with a standard deviation of 3.2% and range of 0.3–10.7%; Fig. 4), the influence of vesicles on rheology is relatively small (Lewellin and Manga 2005; Mader et al. 2013; Truby et al. 2015). The effect of the vesicle fraction varies with strain rate, with relative viscosities for our lavas ranging from 0.9 to 1.1 for η_{app} of 2000 Pa s and an average bubble radius of 0.01 mm following Llewellin and Manga (2005) and Mader et al. (2013). Vesicles in these lavas can therefore decrease or increase the apparent viscosity during flow and can thus be considered to increase uncertainty. For the tephra and spatter samples, the higher vesicularity results in greater uncertainty, but a full vesicle size distribution and independent strain rate analysis is needed to determine the rheology effect more precisely (Mader et al. 2013). However, model results and their errors from both textural and petrologic analyses are representative of the magnitudes and trends in the viscosity results (e.g., Riker et al. 2009; Chevrel et al. 2013; Mader et al. 2013), while also highlighting uncertainties (Fig. 6).

Effusion rates

Effusion rate calculations integrate rheology and morphology datasets using methods from Kerr et al. (2006) and Deardorff and Cashman (2012). As predicted by Eq. 4, channel width shows an inverse relationship with slope (Fig. 7a). However, this relationship does not hold for flow segments where lateral spreading of the flow is limited, such as where the Central and Southern flows wind through hilly topography (Fig. 3). We therefore exclude these regions from our analysis. Local effusion rates through each channel are calculated by fitting Eq. 4 to the remaining morphologic data with rheological parameters derived from our petrologic analysis and solving for the best-fit flux term (Q in Eq. 4).

The rheological parameters that must be determined for application of this crust-dominated flow model are the strength of the crust and the core viscosity. We estimate the crustal yield strength from the 1256 CE rheological parameters and the observed total mean output rate (solid line in Fig. 7a). Fitting Eq. 4 to the 1256 CE total mean output rate, core viscosity, slope, and channel width returns a crustal yield strength of $2.5 \pm 0.5 \times 10^6$ Pa, which falls within the range observed for lavas in other studies (Blake and Bruno 2000; Kerr et al. 2006; Kerr and Lyman 2007; Deardorff and Cashman 2012; Castruccio et al. 2013). The core viscosities derived from the apparent viscosity measurements for each flow are given in Table 5. While our Harrat Rahat measurements generally capture solidification down-flow with lower temperatures and increasing crystal content, the bulk rheology of the 1256 CE flow, as well as the limited Northern flow results, changes little over distance (Figs. 4 and 5).

Fig. 4 a, b SEM BSE images showing textural changes in the 1256 CE flow at the vent (0 km) and down-flow (12 km). c Volume percent of crystals and vesicles with distance down-flow. All samples from the vent area (distance along flow of 0 km) are tephra or spatter samples
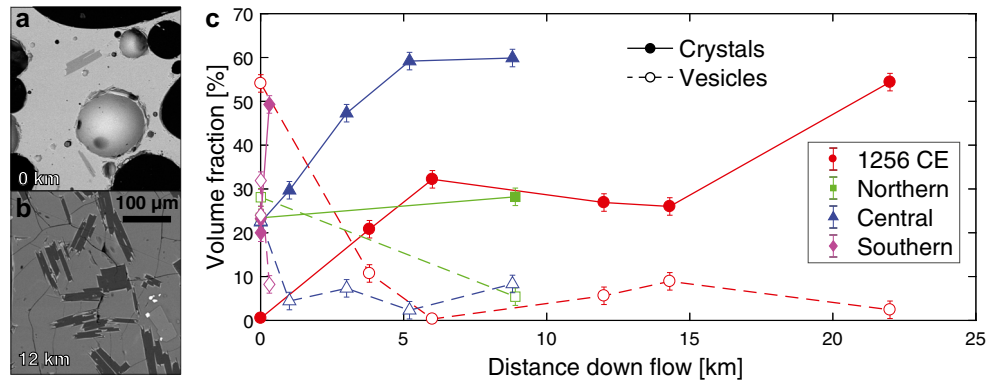
Results for each flow and flow branch show a range in best-fit lava channel fluxes (local effusion rates) based on channel width, rheology, and slope of between 15 ± 2 and $68 \pm 11 \ m^3 \ s^{-1}$ (Table 5). With significant scatter in the data, we include the 95% confidence interval error for fitted flux values in Table 5. Following Deardorff and Cashman (2012), we also further account for this scatter by finding flux values that bracket the entire dataset, including flow width, to explore the full range of potential values (Fig. 7b). Instantaneous effusion rate typically peaks near the start of eruptions (e.g., Wadge 1981; Harris et al. 2011; Bonny and Wright 2017), and flow width may capture this with best-fit fluxes on the order of $100 \ m^3 \ s^{-1}$ (Table 5). Flow width also grows by overflows (e.g., Walker 1971; Lipman and Banks 1987; Tarquini and de' Michieli Vitturi 2014), so these values represent maxima. While our results have significant uncertainty, the magnitudes and relative lava fluxes through these channels provide information on eruption dynamics.

For flows with simple channel geometries (i.e., the cases of the 1256 CE pulse II and the Central flow), the lava flux through a single channel represents an estimate of the total average effusion rate at the vent during channel formation. For branched flow fields (Northern and Southern flow fields), the volumetric lava fluxes of each branch capture the local average effusion rates and should sum to the total average effusion rate at the vent (36 ± 5 and $108 \pm 12 \ m^3 \ s^{-1}$, respectively). For the Northern flow, our results show similar local effusion rates through the western and eastern channels (Table 5). Within the Southern flow, the estimated effusion rate through the southern channel is more than 1.5 times higher than for the northern channel. Morphologically, our mapping shows that only the northernmost section of the eruptive fissure lies directly upslope of the northern channel (Figs. 1b and 3), so this difference could reflect that the northern branch was fed by a smaller proportion of the fissure than the southern branch.

Eruption durations

We can also use these effusion rate estimates to calculate the potential range of eruption durations for the Five Fingers.

Taking the lava flux estimates through the channels as best estimates for the local average effusion rates, in combination with the corresponding volumes of each branch in Table 5, we calculate the time required to emplace the individual flow branches. These emplacement times offer estimates of eruption durations with values on the order of weeks, similar to the 52-day duration of the eruption observed for the entire 1256 CE eruption (Al-Samhoody 1486; Camp et al. 1987). Different durations estimated for the different branches of the Northern and Southern flows suggest that not all branches were active for the entire eruption. For example, the estimated local average effusion rate through the northern channel of the Southern flow is lower than for southern channel, but the volume of the northern branch is larger (Table 5). This may reflect that while the northern branch was fed at a lower lava supply rate, it was fed for a longer duration than the southern branch.

Discussion

By integrating morphologic and textural observations with analytical models of rheology and flow propagation, we can reconstruct the emplacement conditions and behaviors of these mafic volcanic field flows. Results encompass eruption temperatures, viscosities, effusion rates, down-flow cooling and crystallization, as well as eruption duration. All of these inform the dynamics of past Harrat Rahat eruptions and have implications for the magnitudes, rheologies, dynamics, and timescales of mafic volcanic field eruptions. We analyze our results in context through comparisons with other volcanic fields, as well as recent, well-observed mafic lava flows from shield and stratovolcanoes around the world (Table 6).

Cooling and crystallization

The rheological evolution of these Harrat Rahat lava flows demonstrates the interplay between cooling, crystallization, and surface morphology in basaltic lavas. Vent temperatures of ~ 1140 °C calculated for Harrat Rahat lavas are sub-liquidus, as shown by the initial crystallinity at the vent, which

Table 4 Textural analysis, thermometry, and viscosity results

	1256 CE flow						Northern flow	
Sample	R14TS95	R15DD150B	R15DD015	R15DD012	R15DD010	R15HD010	R15DD18	R15DD14
Description	Tephra	Lava	Lava	Lava	Lava	Lava	Spatter	Lava
Distance from vent (km)	0	3.8	6.0	12.0	14.3	22.0	0	8.9
Volume proportions from textural analysis (%)								
Melt	45.3	68.5	67.5	67.5	65.1	43.2	48.5	66.4
Vesicles	54.1	10.7	0.3	5.6	8.9	2.4	28.1	5.4
Crystals	0.5	20.8	32.2	26.9	26.0	54.4	23.4	28.2
Plagioclase	0.2	13.3	24.3	24.0	22.6	48.0	18.9	19.9
Olivine	0.3	7.5	7.4	2.6	3.3	6.2	3.1	8.0
Oxides	0.0	0.0	0.4	0.3	0.1	0.3	1.4	0.4
Thermometry (°C)								
Average	1141	1139	1111	1123	1133	1097	1118	1125
Standard error	6	6	6	5	6	10	5	6
Viscosity (Pa s)								
Liquid viscosity, Giordano et al. (2008)	1.4×10^2	1.4×10^2	4.2×10^2	2.7×10^2	1.9×10^2	7.0×10^2	6.7×10^2	3.1×10^2
Apparent viscosity, Mueller et al. (2011)	1.5×10^2	4.8×10^2	3.2×10^3	1.4×10^3	1.0×10^3	–	5.3×10^3	1.9×10^3
Apparent viscosity, Costa et al. (2009), strain rate of 10^{-4} s^{-1}	1.5×10^2	4.5×10^2	3.4×10^3	1.4×10^3	1.0×10^3	3.4×10^6	5.6×10^3	1.9×10^3
Apparent viscosity, Costa et al. (2009), strain rate of 1 s^{-1}	1.5×10^2	3.8×10^2	2.6×10^3	1.1×10^3	8.2×10^2	1.0×10^6	4.3×10^3	1.5×10^3

	Central flow					Southern flow		
Sample	R16HD01	R16HD14	R16HD13	R16HD15	R16HD16	R16HD09	R16HD27	R16HD26
Description	Spatter	Lava	Lava	Lava	Lava	Spatter	Spatter	Lava
Distance from vent (km)	0	1.0	3.0	5.2	8.8	0	0	0.3
Volume proportions from textural analysis (%)								
Melt	54.9	65.9	45.4	38.5	31.8	56.0	44.9	42.5
Vesicles	22.6	4.4	7.3	2.3	8.3	24.0	31.9	8.2
Crystals	22.4	29.7	47.3	59.2	59.9	20.0	23.2	49.3
Plagioclase	16.4	22.1	36.2	46.4	46.7	13.9	15.7	43.9
Olivine	5.5	6.6	10.1	10.7	8.1	5.9	6.5	3.1
Oxides	0.5	1.0	1.0	2.2	5.1	0.2	1.0	2.3
Thermometry (°C)								
Average	1141	1135	1114	1073	1089	1150	1141	1102
Standard error	6	6	7	9	6	5	6	10
Viscosity (Pa s)								
Liquid viscosity, Giordano et al. (2008)	1.9×10^2	2.0×10^2	5.7×10^2	1.1×10^4	3.8×10^3	9.8×10^1	1.3×10^2	8.0×10^2
Apparent viscosity, Mueller et al. (2011)	1.1×10^3	1.4×10^3	–	–	–	4.3×10^2	1.3×10^3	–
Apparent viscosity, Costa et al. (2009), strain rate of 10^{-4} s^{-1}	1.1×10^3	1.4×10^3	3.9×10^5	5.2×10^8	1.6×10^9	4.2×10^2	1.4×10^3	1.6×10^6
Apparent viscosity, Costa et al. (2009), strain rate of 1 s^{-1}	8.4×10^2	1.1×10^3	1.5×10^5	1.5×10^8	4.1×10^8	3.4×10^2	1.0×10^3	5.2×10^5

Note: See Online Resource 2 for results from individual geothermometers. Viscosity errors are calculated on a log scale and shown as error bars in Fig. 6
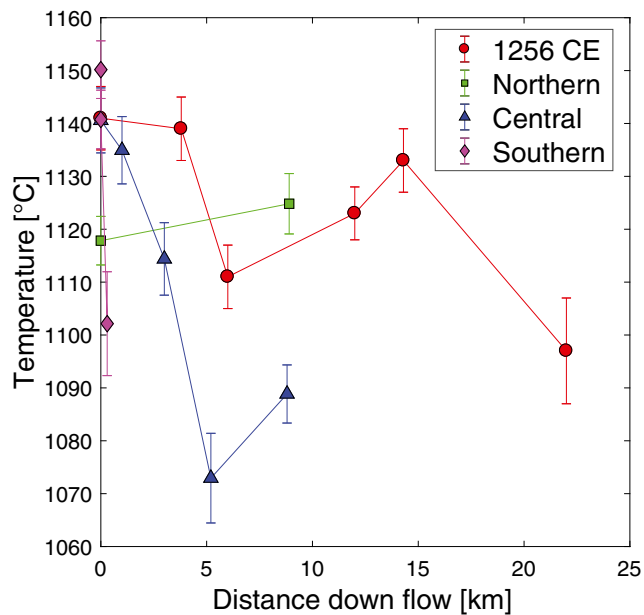
Fig. 5 Temperatures calculated with liquid, olivine-liquid, and plagioclase-liquid geothermometers, with distance down-flow. Values are averages of all temperature calculations (Online Resource 2) and error bars are ± 1 standard error (Table 4)

is in agreement with liquidus temperatures of 1188 to 1223 °C estimated by MELTS at atmospheric pressure (Ghiorso and Sack 1995). Vent temperatures are similar to eruption temperatures of 'a'ā-dominated flows at Mauna Loa and Kīlauea volcanoes in Hawai'i (Table 6; Lipman and Banks 1987; Wolfe et al. 1987; Cashman et al. 1999; Soule et al. 2004; Robert et al. 2014). The 1256 CE flow measurements show an overall cooling rate of 1.6 °C km⁻¹, while the Central flow cooled much more rapidly at 7.0 °C km⁻¹ (Fig. 5). These rates are consistent with open channel flows, where cooling rates, particularly near the vent, can be greater than 5 °C km⁻¹, but cooling along channels more distally can be less than 1 °C km⁻¹ (Table 6; Lipman and Banks 1987; Cashman et al. 1999; Soule et al. 2004; Harris et al. 2007b; Riker et al. 2009; Robert et al. 2014; Kolzenburg et al. 2017;
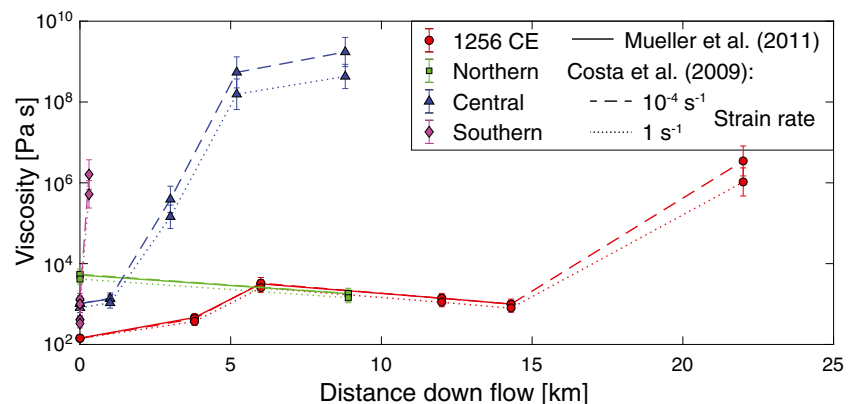
Rhéty et al. 2017). Temperatures at the vent may also have varied during eruption, particularly with variable magma compositions (Table 1), but we are unable to assess this with our samples. For the Northern and Southern flows, cooling trends are uncertain due to the lack of glassy samples from along their lengths. Nevertheless, our sampling enables estimates of vent temperature, with a distal sample from the Northern flow that shows a slight increase in temperature (within error) and a near-vent sample from the Southern flow shows cooling, but with a large uncertainty.

Cooling of the Harrat Rahat flows is accompanied by a dramatic increase in crystallinity, with both olivine and plagioclase crystallizing in the groundmass, which is normal during cooling of basaltic lavas (e.g., Helz and Thornber 1987; Crisp et al. 1994; Soule et al. 2004; Riker et al. 2009; Robert et al. 2014; Rhéty et al. 2017; Soldati et al. 2018). All of the flows record a similar relationship between temperature and crystallinity (Fig. 8). In places, small temperature changes are accompanied by significant crystallization, suggesting degassing-induced crystallization and buffering of flow temperature by latent heat (Lipman and Banks 1987; Riker et al. 2009). The 1256 CE flow shows nearly constant flow temperature and crystallinity over much of its length (Figs. 4 and 5), resulting in steady calculated viscosities (Fig. 6) and supporting the use of the crust-dominated model for effusion rate estimation.

The rheological evolution of each flow is also accompanied by changes in surface morphology. Mapping of the 1256 CE flow by Kereszturi et al. (2016) found a transition from pāhoehoe to 'a'ā at ~2 km down-flow (Fig. 1b). This transition is strongly controlled by viscosity, and the trends in our data suggest a temperature of ~1140 °C and a vesicle-free crystallinity of ~12%, yielding a viscosity of ~250 Pa s, at this distance. These values are consistent with flow properties recorded at the pāhoehoe to 'a'ā transition in a number of Hawaiian flows (Soule et al. 2004; Robert et al. 2014) and rheology experiments (Sehlke et al. 2014; Kolzenburg et al. 2017). Strain rate also plays a major role in the transition, which is often associated with slope increase (e.g., MacDonald 1953; Peterson and Tilling 1980; Robert et al.

Fig. 6 Apparent viscosities with distance down-flow calculated from Eq. 1 with η_{liq} from Giordano et al. (2008) and η_r from Mueller et al. (2011; Eqs. 2 and 3; solid line) or Costa et al. (2009) with parameters from Cimarelli et al. (2011) at low (dashed line) and high (dotted line) strain rates

Fig. 7 **a** The 1256 CE channel width measurements compared to slope with the Eq. 4 curve fit and 95% confidence interval curves (best-fit σ_c of $2.5 \pm 0.5 \times 10^6$ Pa and observed average flux). **b** Flow and channel widths compared to slope for the southern branch of the Southern flow. The best-fit flux is shown in the solid line (68 m³ s⁻¹), accompanied by dashed curves showing 10 and 1000 m³ s⁻¹ fluxes that bracket the dataset
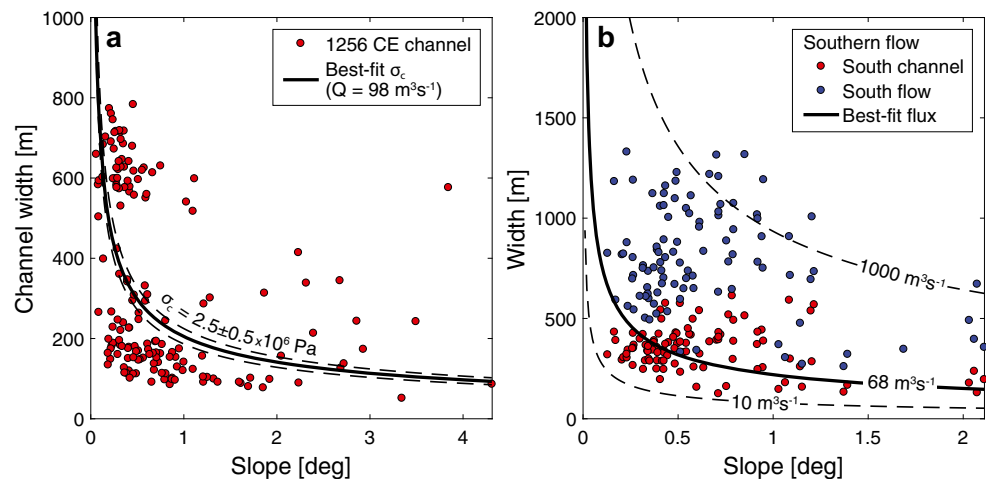
2014). For the 1256 CE flow, we see a large increase in slope (up to 4.3°) at the transition location, accompanied by a decrease in flow thickness and flow width (Fig. 3a, b). Change in slope likely resulted in an increased flow velocity, producing a thinner and narrower flow, as well as higher strain rates that, combined with increased viscosity, formed 'a'ā. Our measurements of rheological and morphological evolution are also in line with the qualitative progression of flow surface morphologies that Murcia et al. (2014) identify in the Five Fingers flows. Further sampling and analysis of the Northern and Southern flows is needed to characterize their rheological evolution more completely.

Flow volumes

Our calculated volumes are similar to past estimates for these Harrat Rahat flows. Previous bulk volume estimates for the 1256 CE flow range from 0.29 to 0.5 km³ (Camp et al. 1987; Murcia et al. 2014; Kereszturi et al. 2016). Our calculation of 0.44 km³ using flow cross-sections accounts for more detail

than an average thickness and total area approach, while also excluding the negative thicknesses within the estimate of 0.4 km³ by Kereszturi et al. (2016). The previous interpretation of the Five Fingers flows as made up of the northern "Two Fingers" (Northern flow) and the southern "Three Fingers" (Central and Southern flows) yielded bulk volumes of 0.09 and 0.23 km³, respectively (Murcia et al. 2014). We calculate a much larger bulk volume of 0.18 km³ for the Northern flow, which is consistent with the area and thicknesses reported in Murcia et al. (2014), whereas the "Three Fingers" volume is similar to our combined bulk volume of Central and Southern flows of 0.20 km³ (0.22 km³ including vents; Table 2). Based on mapping of the entire volcanic field, the extents of these flows are representative of Harrat Rahat basalts (Camp and Roobol 1989; Downs et al. 2018).

With DRE volumes on the order of 10^{-2} to 10^{-1} km³, these Harrat Rahat lavas are small-volume basalts typical of mafic volcanic fields (< 1 km³; Valentine and Connor 2015; Table 6). However, the comparison in Table 6 shows that they have larger volumes than many recent basaltic

Table 5 Effusion rate, duration, and advance rate estimates

Flow	Core viscosity (Pa s)	Best-fit flux (m³ s⁻¹)	Maximum flux from flow width (m³ s⁻¹)	Duration (days)	Average advance rate (m h⁻¹)	Channel advance rate (m h⁻¹)
1256 CE flow	$7.6 \pm 2.0 \times 10^2$	98 (fit)	$7.0 \pm 0.9 \times 10^2$	52 (observed)	17	$8.4 \pm 0.6 \times 10^2$
Northern flow		36 ± 5	$5.7 \pm 1.0 \times 10^2$			
West branch	$2.9 \pm 0.9 \times 10^3$	15 ± 2	$4.0 \pm 1.0 \times 10^2$	108 ± 15	6 ± 1	$2.3 \pm 0.3 \times 10^2$
East branch	$2.9 \pm 0.9 \times 10^3$	21 ± 5	$1.7 \pm 0.4 \times 10^2$	24 ± 6	23 ± 6	$2.7 \pm 0.6 \times 10^2$
Central flow	$4.3 \pm 1.8 \times 10^3$	51 ± 13	$1.8 \pm 0.3 \times 10^2$	15 ± 4	44 ± 11	$2.4 \pm 0.5 \times 10^2$
Southern flow		$1.1 \pm 0.1 \times 10^2$	$6.4 \pm 0.8 \times 10^2$			
North branch	$1.8 \pm 0.8 \times 10^3$	40 ± 5	$3.2 \pm 0.7 \times 10^2$	26 ± 3	32 ± 4	$3.4 \pm 0.5 \times 10^2$
South branch	$1.8 \pm 0.8 \times 10^3$	68 ± 11	$3.2 \pm 0.5 \times 10^2$	8 ± 1	85 ± 13	$4.4 \pm 0.7 \times 10^2$

Table 6 Comparison of Harrat Rahat emplacement conditions to other mafic lava flows

Volcano	Volume (bulk, ×10⁶ m³)	Length (km)	Eruption temperature (°C)	Cooling rate (°C km^{-1})	Effusion rate (m³ s^{-1})	Duration (days)	Advance rate (m h^{-1})	References
Mafic volcanic fields								
Harrat Rahat	70–440	14.3–21.8	1118–1150	1.6–7.0	36–106	15–108	6–840	This paper
Parícutin 1943–1952	700	1–10	1070	–	1–4	0.5	1–180	Krauskopf (1948); Fries (1953); Foshag and González (1956)
Auckland	0.02–650	0.8–11	–	–	–	–	–	Kereszturi et al. (2013)
Cima	15	2	1110	0	30	6	14 (average)	Soldati et al. (2017)
Sand Mountain	1–190	< 8	–	–	–	–	–	Deligne et al. (2016)
Other mafic lava flows								
Mauna Loa	1–383	10–51				1–450		Lockwood and Lipman (1987)
1859	270	51	1194–1216	0.5–5.6	116–235 (391 peak)	18–27	267 (average), 3600 (max)	Riker et al. (2009)
1984	220	27	1140	0.7	275	21	280 (average), 5000 (max)	Lipman and Banks (1987)
Kīlauea								
May 1974	4.1–9.7	8.6	1164	6.7	23–54 (90–420 peak)	2.1	600 (max)	Harris et al. (2009); Robert et al. (2014); Sehlke et al. (2014)
July 1974	3.5	2	1150	7	150–275	0.2	350–6000	Soule et al. (2004)
Puʻu ʻŌʻō (ʻaʻā flows)	2–38	2–13	1135–1150	4.4–6.8	10–500	0.2–16	50–500	Wolfe et al. (1987); Cashman et al. (1999); Helikerz and Mattox (2003); Kauahikaua et al. (2003)
Piton de la Fournaise								
April 2007	200–230	3	1167	6.8–42	84 (200 peak)	29.6	261	Peltier et al. (2009); Rhéty et al. (2017)
December 2010	350	1.1	1145	11–27	9.8 (132 peak)	0.6	73 (average)	Soldati et al. (2018)
Tenerife (historical)	0.7–51	2–9	–	–	0.5–15	9–>98	70–4000	Solana (2012)
Holuhraun 2014–2015	1440	17	1147–1200	18.7–24	90 (350 peak)	182	63	Kolzenburg et al. (2017); Pedersen et al. (2017)
Etna (since 1980)	0.4–185	0.2–8.8	1060–1100	5–180 (max 2001)	0.3–183	0.2–<518	30 (2001)–125 (max, 1981)	Guest et al. (1987); Harris et al. (2005); Coltelli et al. (2007); Harris et al. (2007b); Harris et al. (2011)

Note: Values for whole volcanic fields or volcanoes are ranges for lava flows from them. Effusion rates are bulk mean output rates unless specified

lava flows at Kīlauea (Heliker and Mattox 2003), Piton de la Fournaise (Peltier et al. 2009), Tenerife (Solana 2012), and Etna (Harris et al. 2011), but are of similar volume to historic eruptions from Mauna Loa (Lockwood and Lipman 1987) and smaller than the 2014–2015 Holuhraun eruption in Iceland (Pedersen et al. 2017). Among mafic volcanic fields, these young Harrat Rahat lavas are larger than most Auckland volcanic field lavas
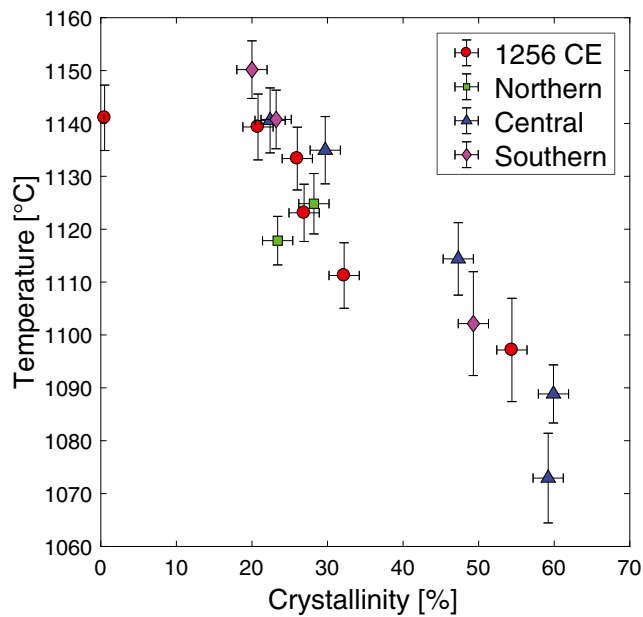
Fig. 8 Calculated temperature versus measured crystallinity for all studied flows

(Kereszturi et al. 2013), smaller than the total eruption of Parícutin (Fries 1953), and of similar size to past eruptions in the Sand Mountain and Cima volcanic fields (Deligne et al. 2016; Soldati et al. 2017).

Flow dynamics

Effusion rate estimates and emplacement timescales are of primary importance for understanding and modeling lava flow behavior (Harris et al. 2007a). Our combined rheologic and morphologic analyses reveal local average effusion rates ranging from 36 to 106 m^3 s^{-1}, erupting over 1 to 15 weeks (Table 5). These effusion rates are typical for Kīlauea 'a'ā flows (Heliker and Mattox 2003; Kauahikaua et al. 2003), consistent with the latter phases of the Holuhraun eruption (Pedersen et al. 2017), larger than most Etna eruptions (Harris et al. 2011), but smaller than many Mauna Loa eruptions (Walker 1973) (Table 6). Among volcanic fields, a similar effusion rate of 10^1 to 10^2 m^3 s^{-1} has been estimated from the youngest eruption within the Cima volcanic field using rheology experiments and morphologic analysis (Soldati et al. 2017), while typical lava effusion during the Parícutin eruption was observed on the order of 1 m^3 s^{-1} (Kraukopf 1948). In Harrat Rahat, calculated eruption durations of weeks are in agreement with the 1256 CE eruption, and similar to observed Mauna Loa, Etna, Tenerife, and Piton de la Fournaise eruptions (Table 6; Lockwood and Lipman 1987; Peltier et al. 2009; Harris et al. 2011; Solana 2012). Our analysis is constrained by the limited glassy samples available and significant uncertainties, but it provides valuable estimates of effusion rates and emplacement durations of Harrat Rahat

eruptions, as well as insights into the magnitudes and time-scales of activity at other mafic volcanic fields.

Lava flow length is widely observed to be controlled by effusion rate, and our data support this. We estimate total average effusion rate and flow length independently for each eruption and find a correlation between them (Fig. 9). Our results fall within the global distribution of basalt flow lengths and average effusion rates (Walker 1973). Although lateral confinement can lengthen flows (Dietterich and Cashman 2014), our results from the Central and Southern flows, which are both confined at their distal ends by interaction with hilly topography, do not show this effect. The geometry of these hills, while laterally confining, may have also impeded the flow advance, forcing the highly sinuous flow paths apparent in the morphology and reducing the anticipated lengthening effect (Fig. 1b).

Flow lengths and estimated eruption durations indicate average advance rates on the order of 6 to 85 m h^{-1} with significant uncertainty (Table 5). Our measurements can also be used to estimate likely velocities within channels during eruption. Channel geometry, slope, flux, and rheology can be related to channel depth-averaged propagation rate (U_{front}) after Kerr et al. (2006):

$$U_{front} = \frac{1}{3}\left[\frac{9g\Delta\rho\sin\theta Q^2}{\mu W^2}\right]^{1/3}. \tag{5}$$

Applying this equation with the core viscosity, calculated flux, and average width and slope, we calculate propagation rates at the flow front of between 230 and 840 m h^{-1} (Table 5), which are faster than average rates from length and duration. These faster velocities may more accurately represent lava advance rates in the early stages of the eruption, and correspond well with advance rates of flows with comparable
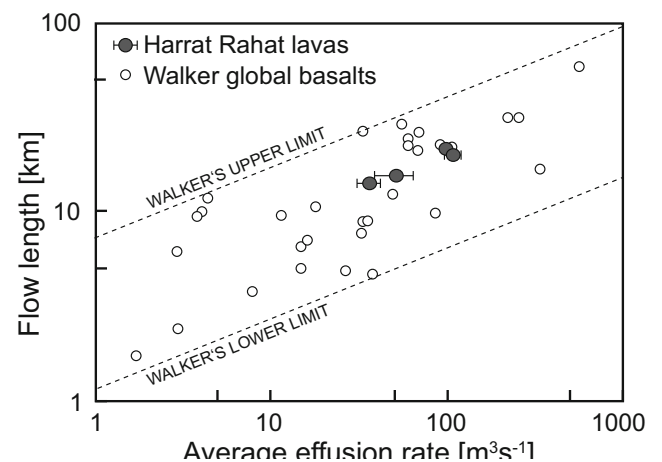

Fig. 9 Length versus effusion rate for the four studied Harrat Rahat lava flows plotted with the global dataset of mean output rates and lengths of basalt lavas and general trend limits from Walker (1973). Effusion rates are the total mean output rate for the 1256 CE flow and the best-fit total average effusion rates from analytical modeling for the Five Fingers flows

effusion rates at other mafic volcanic fields and basaltic shields and stratovolcanoes (Table 6). Modeling of the 1256 CE flow by Kereszturi et al. (2016) similarly found maximum modeled time-averaged advance rates of ~ 200 m h^{-1}. Further from the vent, and later in the eruption, decaying effusion rates and continued cooling and crystallization would have retarded flow advance (e.g., Wadge 1981; Lipman and Banks 1987; Harris and Rowland 2001; Bonny and Wright 2017).

Conclusions

With few observed eruptions in Holocene mafic volcanic fields worldwide, our morphologic and petrologic analyses of lava flow emplacement in Harrat Rahat offer insight into the eruptive conditions and dynamics of these events. We focus on four of the youngest flows in Harrat Rahat and use new whole-rock geochemistry and field observations to separate the previously described Five Fingers into three separate eruptive units, with the Northern and Southern flows made up of multiple flow branches. Morphologic analysis yields volume estimates typical of mafic volcanic fields ranging from 0.07 to 0.42 km^3 DRE. With petrologic analysis, we find that these flows erupted at sub-liquidus temperatures of around 1140 °C. For the well-sampled 1256 CE and Central flows, we observed flow cooling and crystallization with distance down-flow producing apparent viscosities that increased from 10^2 to 10^9 Pa s. Combining rheology estimates with morphologic analysis of channel width and slope, we use analytical theory to reconstruct effusion rates that ranged approximately 40–110 m^3 s^{-1}, and estimate eruption durations of 1–15 weeks. Our results support previous assessments of the intrinsic and extrinsic controls on lava flow emplacement, tracking the temperature and crystallinity down-flow, quantitatively describing the transition from pāhoehoe to ʻaʻā, and documenting the effects of effusion rate and underlying topography on flow morphology and length (e.g., Walker 1973; Cashman et al. 1999; Soule et al. 2004; Riker et al. 2009; Robert et al. 2014; Soldati et al. 2018).

A comparative analysis of these results demonstrates that these mafic monogenetic volcanic field eruptions in Harrat Rahat have similar emplacement conditions to observed basaltic eruptions around the world (Fig. 9; Table 6). We find flow volumes and lengths consistent with other mapped mafic volcanic fields, and additionally contribute estimates of effusion rates and durations that offer quantitative insights into the magnitudes and variability of these crucial eruption parameters in these settings. Our petrology and rheology results record similar behavior to well-studied open channel flows and contribute measurements, trends, and interdependencies of the physical properties of flows in mafic volcanic fields. Critically, we also show that these Harrat Rahat lavas have comparable properties and dynamics to recent eruptions at basaltic shield and stratovolcanoes. Thus, the frequent mafic effusive eruptions in these settings can inform the properties and dynamics of the less frequent, but widespread, mafic volcanic field eruptions for a greater understanding of their eruptive history and potential future behavior.

References

Beattie P (1993) Olivine-melt and orthopyroxene-melt equilibria. Contr Mineral Petr 115:103–111. https://doi.org/10.1007/BF00712982

Bergantz GW, Schleicher JM, Burgisser A (2017) On the kinematics and dynamics of crystal-rich systems. J Geophys Res 122:6131–6159. https://doi.org/10.1002/2017JB014218

Blake S, Bruno BC (2000) Modelling the emplacement of compound lava flows. Earth Planet Sci Lett 184:181–197. https://doi.org/10.1016/S0012-821X(00)00278-8

Bonny E, Wright R (2017) Predicting the end of lava flow-forming eruptions from space. Bull Volcanol 79:52. https://doi.org/10.1007/s00445-017-1134-8

Camp VE, Roobol MJ (1989) The Arabian continental alkali basalt province: part I. Evolution of Harrat Rahat, Kingdom of Saudi Arabia. Geol Soc Am Bull 101:71–95

Camp VE, Roobol MJ (1991) Geologic map of the Cenozoic lava field of Harrat Rahat, Kingdom of Saudi Arabia. Saudi Geological Survey map GM-123

Camp VE, Hooper PR, Roobol MJ, White DL (1987) The Madinah eruption, Saudi Arabia: magma mixing and simultaneous extrusion of three basaltic chemical types. Bull Volcanol 49:489–508

Cashman KV, Thornber C, Kauahikaua J (1999) Cooling and crystallization of lava in open channels, and the transition of pāhoehoe lava to ʻaʻā. Bull Volcanol 61:306–323. https://doi.org/10.1007/s004450050299

Cashman KV, Soule SA, Mackey BH, Deligne NI, Deardorff ND, Dietterich HR (2013) How lava flows: new insights from applications of lidar technologies to lava flow studies. Geosphere 9:1664–1680. https://doi.org/10.1130/GES00706.1

Castruccio A, Rust AC, Sparks RSJ (2013) Evolution of crust- and core-dominated lava flows using scaling analysis. Bull Volcanol 75. https://doi.org/10.1007/s00445-012-0681-2

Castruccio A, Rust AC, Sparks RSJ (2014) Assessing lava flow evolution from post-eruption field data using Herschel–Bulkley rheology. J Volcanol Geoth Res 275:71–84. https://doi.org/10.1016/j.jvolgeores.2014.02.004

Chevrel MO, Guilbaud M, Siebe C (2016) The ~AD 1250 effusive eruption of El Metate shield volcano (Michoacán, Mexico): magma source, crustal storage, eruptive dynamics, and lava

rheology. Bull Volcanol 78:32. https://doi.org/10.1007/s00445-016-1020-9

Chevrel MO, Platz T, Hauber E, Baratoux D, Lavallée Y, Dingwell DB (2013) Lava flow rheology: a comparison of morphological and petrological methods. Earth Planet Sci Lett 384:109–120. https://doi.org/10.1016/j.epsl.2013.09.022

Cimarelli C, Costa A, Mueller S, Mader HM (2011) Rheology of magmas with bimodal crystal size and shape distributions: insights from analog experiments. Geochem Geophys Geosyst 12:Q07024. https://doi.org/10.1029/2011GC003606

Coltelli M, Proietti C, Branca S, Marsella M, Andronico D, Lodato L (2007) Analysis of the 2001 lava flow eruption of Mt. Etna from three-dimensional mapping. J Geophys Res 112:F02029. https://doi.org/10.1029/2006JF000598

Costa A (2005) Viscosity of high crystal content melts: dependence on solid fraction. Geophys Res Lett 32:L22308. https://doi.org/10.1029/2005GL024303

Costa A, Caricchi L, Bagdassarov N (2009) A model for the rheology of particle-bearing suspensions and partially molten rocks. Geochem Geophys Geosyst 10:Q03010. https://doi.org/10.1029/2008GC002138

Crisp J, Cashman KV, Bonini JA, Hougen SB, Pieri DC (1994) Crystallization history of the 1984 Mauna Loa lava flow. J Geophys Res 99:7177–7198. https://doi.org/10.1029/93JB02973

Deardorff ND, Cashman KV (2012) Emplacement conditions of the c. 1, 600-year bp Collier Cone lava flow, Oregon: a LiDAR investigation. Bull Volcanol 74:2051–2066. https://doi.org/10.1007/s00445-012-0650-9

Deligne NI, Conrey RM, Cashman KV, Champion DE, Amidon WH (2016) Holocene volcanism of the upper McKenzie River catchment, central Oregon Cascades, USA. Geo Soc Am Bull 128:1618–1635. https://doi.org/10.1130/B31405.1

Dietterich HR, Cashman KV (2014) Channel networks within lava flows: formation, evolution, and implications for flow behavior. J Geophys Res Earth Surf 119:2014JF003103. https://doi.org/10.1002/2014JF003103

Downs DT, Stelten ME, Champion DE, Dietterich HR, Nawab Z, Zahran H, Hassan K, Shawali J (2018) Volcanic history of the northernmost part of the Harrat Rahat volcanic field, Saudi Arabia. Geosphere 14:1253–1282. https://doi.org/10.1130/GES01625.1

Foshag WF, González J (1956) Birth and development of Parícutin Volcano Mexico. Geol Surv Bull 956-D:335–489

Fries C (1953) Volumes and weights of pyroclastic material, lava, and water erupted by Paricutin volcano, Michoacan, Mexico. Eos Trans AGU 34:603–616. doi:https://doi.org/10.1029/TR034i004p00603

Ghiorso MS, Sack RO (1995) Chemical mass transfer in magmatic processes IV. A revised and internally consistent thermodynamic model for the interpolation and extrapolation of liquid-solid equilibria in magmatic systems at elevated temperatures and pressures. Contr Mineral and Petrol 119:197–212. https://doi.org/10.1007/BF00307281

Giordano D, Russell JK, Dingwell DB (2008) Viscosity of magmatic liquids: a model. Earth Planet Sci Lett 271:123–134. https://doi.org/10.1016/j.epsl.2008.03.038

Griffiths RW (2000) The dynamics of lava flows. Annu Rev Fluid Mech 32:477–518. https://doi.org/10.1146/annurev.fluid.32.1.477

Guest JE, Kilburn CRJ, Pinkerton H, Duncan AM (1987) The evolution of lava flow-fields: observations of the 1981 and 1983 eruptions of Mount Etna, Sicily. Bull Volcanol 49:527–540. https://doi.org/10.1007/BF01080447

Harris A, Rowland S (2001) FLOWGO: a kinematic thermo-rheological model for lava flowing in a channel. Bull Volcanol 63(1):20–44

Harris A, Bailey J, Calvari S, Dehn J (2005) Heat loss measured at a lava channel and its implications for down-channel cooling and rheology. Geol S Am S 396:125–146. https://doi.org/10.1130/0-8137-2396-5.125

Harris AJL, Dehn J, Calvari S (2007a) Lava effusion rate definition and measurement: a review. Bull Volcanol 70(1):1–22. https://doi.org/10.1007/s00445-007-0120-y

Harris A, Favalli M, Mazzarini F, Pareschi MT (2007b) Best-fit results from application of a thermo-rheological model for channelized lava flow to high spatial resolution morphological data. Geophys Res Lett 34:L01301. https://doi.org/10.1029/2006GL028126

Harris AJL, Favalli M, Mazzarini F, Hamilton CW (2009) Construction dynamics of a lava channel. Bull Volcanol 71:459. https://doi.org/10.1007/s00445-008-0238-6

Harris A, Steffke A, Calvari S, Spampinato L (2011) Thirty years of satellite-derived lava discharge rates at Etna: implications for steady volumetric output. J Geophys Res 116:B8. https://doi.org/10.1029/2011JB008237

Harris AJL (2015) Basaltic lava flow hazard. In: Volcanic hazards, risks, and disasters. Elsevier, pp 17–46. https://doi.org/10.1016/B978-0-12-396453-3.00002-2

Heliker C, Mattox TN (2003) The first two decades of the Puʻu ʻŌʻō-Kupaianaha eruption: chronology and selected bibliography. In: Heliker C, Swanson DA, Takahashi TJ (eds) The Puʻu ʻŌʻō-Kupaianaha eruption of Kīlauea Volcano, Hawaiʻi: the first 20 years. US Geol Surv Prof Paper 1676:1–28

Helz RT, Thornber CR (1987) Geothermometry of Kilauea Iki lava lake, Hawaii. Bull Volcanol 49:651–668. https://doi.org/10.1007/BF01080357

Higgins MD (2000) Measurement of crystal size distributions. Amer Min 85:1105–1116. https://doi.org/10.2138/am-2000-8-901

Hulme G (1974) The interpretation of lava flow morphology. Geophys J Int 39(2):361–383

Kauahikaua J, Sherrod DR, Cashman KV, Heliker C, Hon K, Mattox TN, Johnson JA (2003) Hawaiian lava-flow dynamics during the Puu Oo-Kupaianaha eruption: a tale of two decades. In: Heliker C, Swanson DA, Takahashi TJ (eds) The Puʻu ʻŌʻō-Kupaianaha eruption of Kīlauea Volcano, Hawaiʻi: the first 20 years. US Geol Surv Prof Paper 1676:63–87

Kawabata E, Cronin SJ, Bebbington MS, Moufti MRH, El-Masry N, Wang T (2015) Identifying multiple eruption phases from a compound tephra blanket: an example of the AD1256 Al-Madinah eruption, Saudi Arabia. Bull Volcanol 77:6. https://doi.org/10.1007/s00445-014-0890-y

Kereszturi G, Németh K, Cronin SJ, Agustín-Flores J, Smith IEM, Lindsay J (2013) A model for calculating eruptive volumes for monogenetic volcanoes—implication for the quaternary Auckland volcanic field, New Zealand. J Volcanol Geoth Res 266:16–33. https://doi.org/10.1016/j.jvolgeores.2013.09.003

Kereszturi G, Németh K, Moufti MR, Cappello A, Murcia H, Ganci G, Del Negro C, Procter J, Zahran HMA (2016) Emplacement conditions of the 1256 AD Al-Madinah lava flow field in Harrat Rahat, Kingdom of Saudi Arabia—insights from surface morphology and lava flow simulations. J Volcanol Geoth Res 309:14–30. https://doi.org/10.1016/j.jvolgeores.2015.11.002

Kerr RC, Griffiths RW, Cashman KV (2006) Formation of channelized lava flows on an unconfined slope. J Geophys Res 111:B10206. https://doi.org/10.1029/2005JB004225

Kerr RC, Lyman AW (2007) Importance of surface crust strength during the flow of the 1988–1990 andesite lava of Lonquimay Volcano, Chile. J Geophys Res 112:B03209. https://doi.org/10.1029/2006JB004522

Kilburn CRJ, Lopes RMC (1991) General patterns of flow field growth: aa and blocky lavas. J Geophys Res 96:19721–19732. https://doi.org/10.1029/91JB01924

Kolzenburg S, Giordano D, Thordarson T, Höskuldsson A, Dingwell DB (2017) The rheological evolution of the 2014/2015 eruption at Holuhraun, central Iceland. Bull Volcanol 79:45. https://doi.org/10.1007/s00445-017-1128-6

Kolzenburg S, Jaenicke J, Münzer U, Dingwell DB (2018) The effect of inflation on the morphology-derived rheological parameters of lava flows and its implications for interpreting remote sensing data—a case study on the 2014/2015 eruption at Holuhraun, Iceland. J Volcanol Geoth Res 357:200–212. https://doi.org/10.1016/j.jvolgeores.2018.04.024

Krauskopf KB (1948) Lava movement at Parícutin Volcano, Mexico. Geol Soc Am Bull 59:1267–1284. https://doi.org/10.1130/0016-7606(1948)59[1267:LMAPVM]2.0.CO;2

Llewellin EW, Manga M (2005) Bubble suspension rheology and implications for conduit flow. J Volcanol Geoth Res 143:205–217. https://doi.org/10.1016/j.jvolgeores.2004.09.018

Lipman P, Banks N (1987) A'a flow dynamics, Mauna Loa 1984. In: Decker RW, Wright TL, Stauffer PH (eds) Volcanism in Hawaii. US Geol Surv Prof Paper 1350:1527–1567

Lockwood JP, Lipman PW (1987) Holocene eruptive history of Mauna Loa Volcano. In: Decker RW, Wright TL, Stauffer PH (eds) Volcanism in Hawaii. US Geol Surv Prof Paper 1350:509–535

Loock S, van Wyk de Vries B, Hénot J (2010) Clinker formation in basaltic and trachybasaltic lava flows. Bull Volcanol 72:859–870. https://doi.org/10.1007/s00445-010-0362-y

Lyman AW, Kerr RC (2006) Effect of surface solidification on the emplacement of lava flows on a slope. J Geophys Res 111:B05206. https://doi.org/10.1029/2005JB004133

Macdonald GA (1953) Pahoehoe, aa, and block lava. Am J Sci 251:169–191. https://doi.org/10.2475/ajs.251.3.169

Mader HM, Llewellin EW, Mueller SP (2013) The rheology of two-phase magmas: a review and analysis. J Volcanol Geoth Res 257:135–158. https://doi.org/10.1016/j.jvolgeores.2013.02.014

Maron SH, Pierce PE (1956) Application of ree-eyring generalized flow theory to suspensions of spherical particles. J Colloid Sci 11:80–95. https://doi.org/10.1016/0095-8522(56)90023-X

Mazzarini F, Pareschi MT, Favalli M, Isola I, Tarquini S, Boschi E (2005) Morphology of basaltic lava channels during the Mt. Etna September 2004 eruption from airborne laser altimeter data. Geophys Res Lett 32:L04305. https://doi.org/10.1029/2004GL021815

Montierth C, Johnston AD, Cashman KV (1995) An empirical glass-composition-based geothermometer for Mauna Loa lavas. In: Rhodes JM, Lockwood JP (eds) Mauna Loa revealed: structure, composition, history, and hazards. Geophysical Monograph, vol 92. Am Geophys Union, Washington, DC, pp 207–217

Moufti MR, Moghazi AM, Ali KA (2012) Geochemistry and Sr–Nd–Pb isotopic composition of the Harrat Al-Madinah volcanic field, Saudi Arabia. Gondwana Res 21:670–689. https://doi.org/10.1016/j.gr.2011.06.003

Moufti MR, Moghazi AM, Ali KA (2013) 40Ar/39Ar geochronology of the Neogene-Quaternary Harrat Al-Madinah intercontinental volcanic field, Saudi Arabia: implications for duration and migration of volcanic activity. J Asian Earth Sci 62:253–268. https://doi.org/10.1016/j.jseaes.2012.09.027

Mueller S, Llewellin EW, Mader HM (2011) The effect of particle shape on suspension viscosity and implications for magmatic flows. Geophys Res Lett 38:L13316. https://doi.org/10.1029/2011GL047167

Murcia H, Németh K, Moufti MR, Lindsay JM, El-Masry N, Cronin SJ, Qaddah A, Smith IEM (2014) Late Holocene lava flow morphotypes of northern Harrat Rahat, Kingdom of Saudi Arabia: implications for the description of continental lava fields. J Asian Earth Sci 84:131–145. https://doi.org/10.1016/j.jseaes.2013.10.002

Murcia H, Lindsay JM, Németh K, Smith, IEM, Cronin SJ, Moufti MRH, El-Masry NN, Niedermann S (2017) Geology and geochemistry of Late Quaternary volcanism in northern Harrat Rahat, Kingdom of Saudi Arabia: implications for eruption dynamics, regional stratigraphy and magma evolution. In: Monogenetic volcanism. Geol Soc

Spec Publ 446 London, pp 173–204. doi:https://doi.org/10.1144/SP446.2

Newman S, Lowenstern JB (2002) VolatileCalc: a silicate melt–H_2O–CO_2 solution model written in Visual Basic for Excel. Comput Geosci 28:597–604. https://doi.org/10.1016/S0098-3004(01)00081-4

Pedersen GBM, Höskuldsson A, Dürig T, Thordarson T, Jónsdóttir I, Riishuus MS, Óskarsson BV, Dumont S, Magnusson E, Gudmundsson MT, Sigmundsson F, Drouin VJPB, Gallagher C, Askew R, Gudnason J, Moreland WM, Nikkola P, Reynolds HI, Schmith J (2017) Lava field evolution and emplacement dynamics of the 2014–2015 basaltic fissure eruption at Holuhraun, Iceland. J Volcanol Geoth Res 340:155–169. https://doi.org/10.1016/j.jvolgeores.2017.02.027

Peltier A, Bachèlery P, Staudacher T (2009) Magma transport and storage at Piton de La Fournaise (La Réunion) between 1972 and 2007: a review of geophysical and geochemical data. J Volcanol Geoth Res 184:93–108. https://doi.org/10.1016/j.jvolgeores.2008.12.008

Peterson DW, Tilling RI (1980) Transition of basaltic lava from pahoehoe to aa, Kilauea Volcano, Hawaii: field observations and key factors. J Volcanol Geoth Res 7:271–293. https://doi.org/10.1016/0377-0273(80)90033-5

Pinkerton H, Wilson L (1994) Factors controlling the lengths of channel-fed lava flows. Bull Volcanol 56:108–120. https://doi.org/10.1007/BF00304106

Putirka KD (2008) Thermometers and barometers for volcanic systems. Rev Mineral Geochem 69:61–120. https://doi.org/10.2138/rmg.2008.69.3

Putirka KD, Perfit M, Ryerson FJ, Jackson MG (2007) Ambient and excess mantle temperatures, olivine thermometry, and active vs. passive upwelling. Chem Geol 241:177–206. https://doi.org/10.1016/j.chemgeo.2007.01.014

Rhéty M, Harris A, Villeneuve N, Gurioli L, Médard E, Chevrel O, Bachélery P (2017) A comparison of cooling-limited and volume-limited flow systems: examples from channels in the Piton de la Fournaise April 2007 lava-flow field. Geochem Geophys Geosys 18:3270–3291. https://doi.org/10.1002/2017GC006839

Riker JM, Cashman KV, Kauahikaua JP, Montierth CM (2009) The length of channelized lava flows: insight from the 1859 eruption of Mauna Loa Volcano, Hawai'i. J Volcanol Geoth Res 183:139–156. https://doi.org/10.1016/j.jvolgeores.2009.03.002

Robert B, Harris A, Gurioli L, Médard E, Sehlke A, Whittington A (2014) Textural and rheological evolution of basalt flowing down a lava channel. Bull Volcanol 76:824. https://doi.org/10.1007/s00445-014-0824-8

Sehlke A, Whittington A, Robert B, Harris A, Gurioli L, Médard E (2014) Pahoehoe to 'a'a transition of Hawaiian lavas: an experimental study. Bull Volcanol 76:876. https://doi.org/10.1007/s00445-014-0876-9

Shea T, Houghton BF, Gurioli L, Cashman KV, Hammer JE, Hobden BJ (2010) Textural studies of vesicles in volcanic rocks: an integrated methodology. J Volcanol Geoth Res 190:271–289. https://doi.org/10.1016/j.jvolgeores.2009.12.003

Siebert L, Simkin T, Kimberly P (2010) Volcanoes of the world, third edn. University of California Press, Washington, DC

Siebert L, Cottrell E, Venzke E, Andrews B (2015) Chapter 12–Earth's volcanoes and their eruptions: an overview. In: Sigurdsson H (ed) The encyclopedia of volcanoes, second edn. Academic Press, Amsterdam, pp 239–255. https://doi.org/10.1016/B978-0-12-385938-9.00012-2

Sisson TW, Grove TL (1993) Temperatures and H_2O contents of low-MgO high-alumina basalts. Contr Mineral and Petrol 113:167–184. https://doi.org/10.1007/BF00283226

Smith IEM, Németh K (2017) Source to surface model of monogenetic volcanism: a critical review. In: Monogenetic volcanism. Geol Soc

Spec Publ 446 London, pp 173–204. doi:https://doi.org/10.1144/SP446.14

Solana MC (2012) Development of unconfined historic lava flow fields in tenerife: implications for the mitigation of risk from a future eruption. Bull Volcanol 74(10):2397–2413

Soldati A, Beem J, Gomez F, Huntley JW, Robertson T, Whittington A (2017) Emplacement dynamics and timescale of a Holocene flow from the Cima volcanic field (CA): insights from rheology and morphology. J Volcanol Geoth Res 347:91–111. https://doi.org/10.1016/j.jvolgeores.2017.09.005

Soldati A, Harris AJL, Gurioli L, Villeneuve N, Rhéty M, Gomez F, Whittington A (2018) Textural, thermal, and topographic constraints on lava flow system structure: the December 2010 eruption of Piton de la Fournaise. Bull Volcanol 80(10)

Soule SA, Cashman KV, Kauahikaua JP (2004) Examining flow emplacement through the surface morphology of three rapidly emplaced, solidified lava flows, Kīlauea Volcano, Hawai'i. Bull Volcanol 66:1–14. https://doi.org/10.1007/s00445-003-0291-0

Stelten ME, Downs DT, Dietterich HR, Mahood GA, Calvert AT, Sisson TW, Zahran H, Shawali J (2018) Timescales of magmatic differentiation from alkali basalt to trachyte within the Harrat Rahat volcanic field, Kingdom of Saudi Arabia. Contrib Mineral Petrol 173:68. https://doi.org/10.1007/s00410-018-1495-9

Stevens NF (2002) Emplacement of the large andesite lava flow in the Oturere Stream valley, Tongariro Volcano, from airborne interferometric radar. New Zeal J Geol Geop 45:387–394. https://doi.org/10.1080/00288306.2002.9514980

Tarquini S, de' Michieli Vitturi M (2014) Influence of fluctuating supply on the emplacement dynamics of channelized lava flows. Bull Volcanol 76:801. https://doi.org/10.1007/s00445-014-0801-2

Truby JM, Mueller SP, Llewellin EW, Mader HM (2015) The rheology of three-phase suspensions at low bubble capillary number. Proc R Soc A 471:20140557. https://doi.org/10.1098/rspa.2014.0557

Valentine GA, Connor CB (2015) Chapter 23—Basaltic volcanic fields. In: Sigurdsson H (ed) The encyclopedia of volcanoes, second edn. Academic Press, Amsterdam, pp 423–439

Wadge G (1981) The variation of magma discharge during basaltic eruptions. J Volcanol Geoth Res 11:139–168. https://doi.org/10.1016/0377-0273(81)90020-2

Walker GPL (1971) Compound and simple lava flows and flood basalts. Bull Volcanol 35:579–590. https://doi.org/10.1007/BF02596829

Walker GPL (1973) Lengths of lava flows. Phil Trans R Soc A 274:107–118. https://doi.org/10.1098/rsta.1973.0030

Walker GPL (2000) Basaltic volcanoes and volcanic systems. In: Sigurdsson H (ed) The encyclopedia of volcanoes. Academic Press, Amsterdam, pp 283–289

Wolfe EW, Garcia MO, Jackson DB, Koyanagi RY, Neal CA, Okamura AT (1987) The Puu Oo eruption of Kilauea Volcano, episodes 1–20, January 3, 1983, to June 8, 1984. In: Decker RW, Wright TL, Stauffer PH (eds) Volcanism in Hawaii. US Geol Surv Prof Paper 1350:471–508